J. Fluid Mech. (1995), *vol.* 288, *pp.* 123–155

Unsteady flow interactions between an advected cylindrical vortex tube and a spherical particle

By INCHUL KIM, SAID ELGHOBASHI AND WILLIAM A. SIRIGNANO

Department of Mechanical and Aerospace Engineering, University of California, Irvine, CA 92717, USA

(Received 5 November 1993 and in revised form 22 October 1994)

The unsteady, three-dimensional, incompressible, viscous flow interactions between a vortical (initially cylindrical) structure advected by a uniform free stream and a spherical particle held fixed in space is investigated numerically for a range of particle Reynolds numbers $20 \leqslant Re \leqslant 100$. The counter-clockwise rotating vortex tube is initially located ten sphere radii upstream from the sphere centre. The finite-difference computations yield the flow properties and the temporal distributions of lift, drag, and moment coefficients of the sphere. Initially, the lift force is positive owing to the upwash on the sphere, then becomes negative owing to the downwash as the vortex tube passes the sphere. Varying the size of the vortex core (σ) shows that the r.m.s. lift coefficient is linearly proportional to the circulation of the vortex tube at small values of σ. At large values of σ, the r.m.s. lift coefficient is linearly proportional to the maximum fluctuation velocity (v_{max}) induced by the vortex tube but independent of σ. For intermediate values of σ, the r.m.s. lift coefficient depends on both σ and v_{max} (or equivalently both σ and the circulation). We observe some interesting flow phenomena in the near wake as a function of time owing to the passage of the vortex tube.

1. Introduction

This paper is concerned with the unsteady, three-dimensional, incompressible, viscous flow interactions between a vortical structure (initially cylindrical) advected by a uniform free stream and a spherical solid particle which is held fixed in space. This flow is equivalent to that of a spherical particle moving along a straight line and traversing the vortical structure at constant velocity. The particle Reynolds number based on the free-stream velocity and particle diameter is in the range $20 \leqslant Re \leqslant 100$. We obtain the unsteady velocity and pressure distributions via the numerical solution of the time-dependent three-dimensional Navier–Stokes equations within a spherical domain surrounding the sphere and the moving vortex tube.

The motivation for studying this flow is the need to understand how the forces (drag, lift and torque) imparted on a particle are influenced by fluctuations in the velocity and pressure of the carrier flow as is the case in particle-laden turbulent flows. Knowledge of the time-dependence of these forces and the unsteady flow field is essential for the accurate calculation of the particle trajectory and the heat and mass transfer rate of the particle (or droplet) which in turn is a prerequisite for predicting particle dispersion and vaporization rate in turbulent flows. The exact relations between these forces and the turbulent fluctuations cannot be obtained analytically owing to the nonlinearity of the equations governing the motion of the particle and fluid. While the cylindrical

vortex is far too simple to represent real turbulence, some important elementary understanding can result from this study.

Numerical simulation of the dispersion of particles in a turbulent flow requires the solution of the equation of particle motion. This equation which is classically known as the Basset–Boussinesq–Oseen (BBO) equation and has been re-derived recently by Maxey & Riley (1983) is restricted to low Reynolds number $Re \leqslant 1$, where $Re = d'|\boldsymbol{u}' - \boldsymbol{v}'|/\nu'$; $\boldsymbol{v}'$ and $\boldsymbol{u}'$ are the velocities of the particle and its surrounding fluid respectively, d' is the particle diameter, and ν' is the fluid kinematic viscosity. Furthermore, the drag force in that equation consists of two terms, namely, the quasi-steady Stokes drag and the unsteady memory term (Basset). The former is purely viscous, whereas the latter depends on both the viscosity and particle acceleration relative to the fluid. The superposition of these two terms is a result of the linearization of the Navier–Stokes equations by Basset (1888). A more serious restriction (than $Re \ll 1$) in the equation of particle motion is that the velocity gradients in the carrier flow in the neighbourhood of the particle should be very small. This requires that the shear Reynolds number $= (a'^2/\nu')(U_0'/L') \ll 1$, where a' is the particle radius, and (U_0'/L') is a reference gradient of the undisturbed velocity field. Therefore, the interesting case in which the eddy (or vortex) size is comparable to that of the particle cannot be properly treated by the standard equation of particle motion. This situation, in addition to being relevant to the fundamental understanding of fluid dynamics, is of practical interest as well. For example, in a typical gas turbine combustor where the Reynolds number is of the order of 10^5 and the integral lengthscale is of the order of 0.1 m, the smallest (Kolmogorov) lengthscale, η, is about 100 μ, which is comparable to the size of a typical fuel droplet. Fluid motion at the Kolmogorov lengthscale experiences the largest strain rates and scalar gradients in the flow. The largest scalar gradients control the important phenomena of heat and mass transfer and chemical reaction. Motion at the largest lengthscales ($\gg \eta$) contains most of the turbulence energy and governs the dispersion of particles (or droplets) but not the small-scale phenomena mentioned above.

Almost all application-oriented studies of diluted particle suspension calculate the drag on the particle using the standard drag curve. This drag curve has been obtained (experimentally and numerically) for a particle fixed in space subjected to a steady flow. In the case of unsteady flow, this drag relationship is an approximation that can be valid only if the timescale of the particle motion is much larger than that of the flow. Note that empirical relationships for unsteady drag have been proposed (e.g. Houghton 1963; Odar 1966; Schöneborn 1975; Ingebo 1956). The expression of Ingebo, derived experimentally, is valid only for the limited conditions of the experiment. All other expressions concern mainly purely harmonic flows. Additional interactions between the particle and the flow are the well-known Saffman's lift due to uniform shear (1965, 1968) and the lift due to particle rotation (Rubinow & Keller 1961). Saffman's lift force expression is valid only for $Re \ll R_{shear}^{1/2}$ and $R_{shear} \ll 1$, where $R_{shear} = (\mathrm{d}u'/\mathrm{d}y')d'^2/(4\nu')$. Under these conditions, the lift due to particle rotation is negligible (Saffman 1965). Recently, McLaughlin (1991) removed the restriction $Re \ll R_{shear}^{1/2}$ and provided a new form for the lift force.

Three-dimensional flow interactions between a vortical structure and a bluff body (a rigid sphere in the simplest form) at finite Reynolds number have not been investigated yet. Our present approach, outlined at the beginning of this section, is a first step toward better understanding of the physics of interaction between a particle and the carrier turbulent flow. For example, we examine the details of the temporal behaviour of the flow structure around the sphere owing to the passage of the vortex tube.

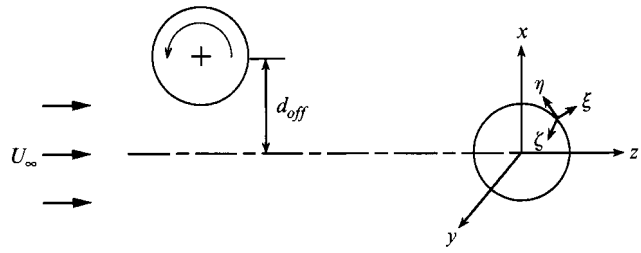

FIGURE 1. Flow geometry and coordinates.

Furthermore, we study the effect of varying the ratio of vortex tube size to particle size, Reynolds number, and offset distance between the particle and the vortex tube on the temporal distributions of the forces imparted on the particle (drag, lift and torque) and the flow structure in the neighbourhood of the particle.

The next section provides a mathematical description of the flow considered, the governing equations and the numerical solution procedure. Section 3 discusses the results including the numerical accuracy issues and the effects of varying the parameters listed above. Section 4 provides a summary of the work.

2. Problem statement and formulation

2.1. *The flow description*

We consider the time-dependent, three-dimensional, incompressible, viscous flow interactions between an initially cylindrical vortex tube and a spherical solid particle. The vortex tube is moving with the laminar free stream, and a sphere is suddenly placed and held fixed in space as shown in figure 1. The initial offset distance, d_{off}, denotes the shortest distance, normalized by the sphere radius, between the initial vortical axis and the (y,z)-plane, which is parallel to the free stream. All the variables are non-dimensionalized using the sphere radius a_0' as the characteristic length and U_∞' as the characteristic velocity, where the superscript $'$ denotes dimensional quantity. The cylindrical vortex tube, whose diameter is of the order of the sphere diameter, is initially located ten radii upstream from the centre of the sphere. The effects of the vortex tube on the sphere are negligible at this initial distance because the magnitude of the initial velocity field induced by the vortex tube is less than 2% of the free-stream velocity. Far upstream, the flow is uniform with constant velocity $U_\infty' \boldsymbol{k}$ parallel to the (y,z)-plane. We have one symmetry plane, the (x,z)-plane, as seen in figure 1.

Two coordinate systems are used in our formulation: the Cartesian coordinates (x,y,z) and the non-orthogonal generalized coordinates (ξ,η,ζ). The origin of the former coincides with the sphere centre. ξ is the radial, η is the angular, and ζ is the azimuthal coordinates. The non-orthogonal generalized coordinate system can be easily adapted to three-dimensional arbitrary geometries. In the present study, a spherical domain is used, and the grid reduces to an orthogonal, spherical grid. The grids are denser near the surface of the spherical particle, and the grid density in the radial direction is controlled by the stretching function developed by Vinokur (1983). Owing to symmetry, the physical domain is reduced to a half spherical space. The domain of the flow is bounded by $1 \leqslant \xi \leqslant N_1$, $1 \leqslant \eta \leqslant N_2$, $1 \leqslant \zeta \leqslant N_3$, where $\xi = 1$ and N_1 correspond, respectively, to the sphere surface and the far-field boundary surrounding the sphere; $\eta = 1$ and N_2 denote, respectively, the positive z-axis and the negative z-axis; $\zeta = 1$ and N_3 refer, respectively, to the (x,z)-plane in the positive

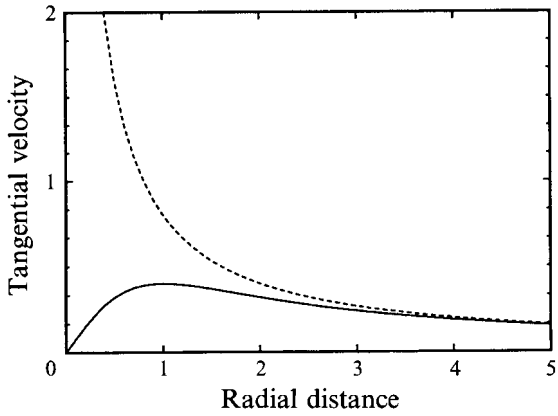

FIGURE 2. Comparison of tangential velocities induced by ---, a point vortex and ——, a vortex tube for $\Gamma_v = 2.5$ and $\sigma = 1$.

x-direction and the (x, z)-plane in the negative x-direction. Uniform spacing ($\delta\xi = \delta\eta = \delta\zeta = 1$) is used, for convenience, for the generalized coordinates.

2.2. *The vortex tube features*

The initial vortex tube has a small core region with a radius σ (normalized by the sphere radius). This core is defined such that the initial velocity induced by the vortex tube approaches zero as the distance from the centre of the vortex tube goes to zero, and at distances much greater than σ, the induced velocity approaches that of a point vortex (figure 2). We use the vortex tube construction of Spalart (1982), which has the following stream function:

$$\psi_v(x, z, t = 0) = -\frac{\Gamma_v}{2\pi} \ln [(x - x_0)^2 + (z - z_0)^2 + \sigma^2], \tag{1}$$

where Γ_v is the non-dimensional circulation around the vortex tube at radius σ and at the initial time. Γ_v is positive when the vortex tube rotates counterclockwise, and x_0 and z_0 denote the location of the centre of the vortex tube. The circulation around a circular path far away from the centre of the vortex is given by $\Gamma_t = 2\Gamma_v$. The tangential velocity distribution of the vortex tube compared with a point vortex is shown in figure 2 for $\Gamma_v = 2.5$ and $\sigma = 1.0$. As shown in figure 2, the cylindrical vortex tube can be viewed as an evolution from the point vortex owing to the cylindrical viscous diffusion. The initial pressure field due to the vortex tube is obtained by solving the radial component of the Navier–Stokes equations which balances the centrifugal acceleration and the pressure gradient for circular streamlines, and has the following form

$$p_v(x, z, t = 0) = -\frac{\Gamma_v^2}{2\pi^2} \frac{1}{(x - x_0)^2 + (z - z_0)^2 + \sigma^2}, \tag{2}$$

where p_v is non-dimensional pressure defined by $p_v = (p'_v - p'_\infty)/\rho' U'^2$. The pressure due to the vortex tube attains its lowest value, $p_{v,\,min} = -\Gamma_v^2/(2\pi^2\sigma^2)$, at the centre of the vortex tube and approaches zero at far distances from the centre of the vortex. Equation (2) is used to prescribe only the initial pressure field generated by the vortex tube.

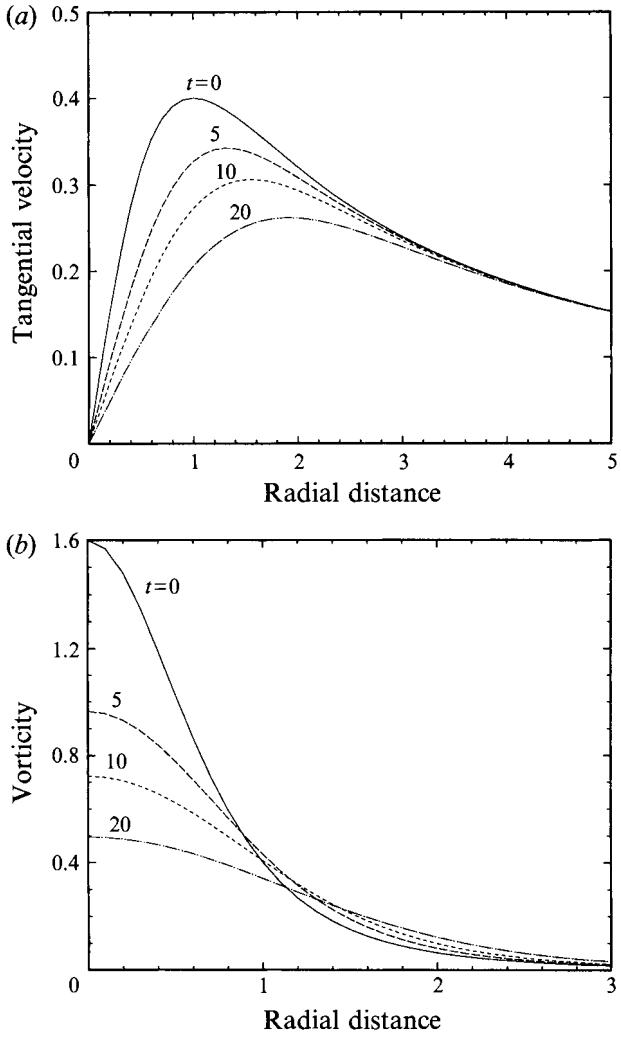

FIGURE 3. (*a*) Velocity and (*b*) vorticity fields due to a vortex tube as a function of radial distance and time for $Re = 100$, $\Gamma_v = 2.5$ and $\sigma = 1$.

In order to gain insight about the properties of the vortex tube, we examine the flow field generated in the absence of the particle. We compute the induced velocity and vorticity field as a function of radius and time owing to the vortex tube moving with the free stream ($U'_\infty \boldsymbol{k}$). The origins of the moving coordinate system is the centre of the vortex tube. We solve the following linear diffusion equation which is the tangential component of the Navier–Stokes equations balancing the unsteady and diffusion terms for the tangential momentum (Batchelor 1967),

$$\frac{\partial u_\theta}{\partial t} = \frac{2}{Re}\left(\frac{\partial^2 u_\theta}{\partial R^2} + \frac{1}{R}\frac{\partial u_\theta}{\partial R} - \frac{u_\theta}{R^2}\right), \tag{3}$$

where R is the radial distance from the centre of the vortex tube, u_θ is the tangential velocity around the vortex tube normalized by the free-stream velocity, and Re is the Reynolds number based on the reference lengthscale a'_0 and the free-stream velocity. Figures 3(*a*) and 3(*b*) show, respectively, the velocity and vorticity fields as a function

of radial distance and time for $Re = 100$, $\Gamma_v = 2.5$, and $\sigma = 1.0$. The size of the vortex core becomes larger as time increases owing to viscous diffusion, whereas the magnitudes of the tangential velocity and the vorticity inside the vortex core decrease. Note that this classical linearized analysis is not employed in the present study; rather a fully nonlinear computational analysis is performed.

2.3. *Governing equations and boundary conditions*

The continuity and momentum equations and the initial and boundary conditions are non-dimensionalized using the sphere radius a_0' as the characteristic length and U_∞' as the characteristic velocity.

$$\nabla \cdot V = 0. \tag{4}$$

$$\frac{\partial V}{\partial t} + \nabla \cdot (VV) = -\nabla p + \frac{2}{Re} \nabla^2 V. \tag{5}$$

The governing equations (4) and (5) are cast in terms of the generalized coordinates (ξ, η, ζ) to treat a three-dimensional body of arbitrary shape. The numerical integration is performed using a cubic computational mesh with equal spacing ($\delta\xi = \delta\eta = \delta\zeta = 1$).

The velocities on the sphere surface are zero owing to the no-slip condition, and the pressure on the sphere is obtained from the momentum equation. The boundary conditions are

$$\frac{\partial p}{\partial n} = \frac{2}{Re} \frac{\partial^2 V_n}{\partial n^2}, \quad u = v = w = 0 \quad \text{at } \xi = 1, \tag{6}$$

$$p = 0, \quad u = v = 0, \quad w = 1 \quad \text{at } \xi = N_1, \quad N_{2mid} \leqslant \eta \leqslant N_2 \text{(upstream)}, \tag{7}$$

$$p = 0, \quad \frac{\partial u}{\partial \xi} = \frac{\partial v}{\partial \xi} = \frac{\partial w}{\partial \xi} = 0 \quad \text{at } \xi = N_1, \quad 1 \leqslant \eta < N_{2mid} \text{(downstream)}, \tag{8}$$

$$\frac{\partial p}{\partial \zeta} = \frac{\partial u}{\partial \zeta} = \frac{\partial w}{\partial \zeta} = 0, \quad v = 0 \quad \text{at } \zeta = 1, \quad N_3, \tag{9}$$

where u, v, and w are the velocities in the x-, y-, and z-directions, respectively, V_n is the velocity in the direction normal to the sphere surface, and p is the pressure. n denotes the direction normal to the sphere surface, $\partial/\partial n = (\xi_x^2 + \xi_y^2 + \xi_z^2)^{1/2} \partial/\partial\xi$, and $\eta = N_{2mid}$ denotes the mid-plane between $\eta = 1$ and N_2. Equation (9) corresponds to the symmetry conditions and zero v velocity in the (x, z) symmetry plane. Conditions guaranteeing continuity in the η direction for p, u, v and w on the axes $\eta = 1$ and $\eta = N_2$ are also imposed.

In order to start the numerical solution of equations (4) and (5), we provide initial velocity and pressure fields by superposing the flow fields due to the uniform stream and the vortex tube in addition to the no-slip condition on the sphere surface:

$$p_0 = p_v, \quad u_0 = -\frac{\partial \psi_v}{\partial z}, \quad v_0 = 0, \quad w_0 = 1 + \frac{\partial \psi_v}{\partial x} \quad \text{except at } \xi = 1, \tag{10}$$

$$p_0 = p_v, \quad u_0 = v_0 = w_0 = 0 \quad \text{at } \xi = 1, \tag{11}$$

where ψ_v and p_v are given by equations (1) and (2), respectively.

The only non-dimensional groupings appearing in the equations and initial and boundary constraints are the sphere Reynolds number, vortex tube radius, offset distance, and vortex circulation (or vortex Reynolds number).

The drag, lift and moment coefficients are evaluated in dimensional form as follows.

$$F'_D = \int_S -p'\boldsymbol{n}\cdot\boldsymbol{k}\,\mathrm{d}S' + \int_S \boldsymbol{n}\cdot\boldsymbol{\tau}'\cdot\boldsymbol{k}\,\mathrm{d}S', \tag{12}$$

$$F'_L = \int_S -p'\boldsymbol{n}\cdot\boldsymbol{i}\,\mathrm{d}S' + \int_S \boldsymbol{n}\cdot\boldsymbol{\tau}'\cdot\boldsymbol{i}\,\mathrm{d}S', \tag{13}$$

$$M' = \int_S \boldsymbol{r}'\times\boldsymbol{\tau}'\,\mathrm{d}S', \tag{14}$$

where S' denotes the surface of the sphere, $\boldsymbol{n}$ is the outward unit normal vector at the surface, $\boldsymbol{r}'$ is the position vector from the centre of the sphere, and $\boldsymbol{\tau}'$ is the viscous stress tensor. The lift force is assumed positive when it is directed toward the positive x-axis. Owing to symmetry, only the y-component of the moment is non-zero and is assumed positive in counter-clockwise direction.

The non-dimensional coefficients of drag, lift and moment are defined, respectively, as

$$C_D = \frac{F'_D}{\frac{1}{2}\rho' U'^2_\infty \pi a'^2_0}, \tag{15}$$

$$C_L = \frac{F'_L}{\frac{1}{2}\rho' U'^2_\infty \pi a'^2_0}, \tag{16}$$

$$C_M = \frac{M'\cdot j}{\frac{1}{2}\rho' U'^2_\infty \pi a'^3_0}. \tag{17}$$

Note that in this analysis, the sphere does not accelerate or rotate owing to the aerodynamic forces and torque.

2.4. *Numerical solution*

We have developed a three-dimensional, implicit, finite-difference algorithm to solve simultaneously the set of the discretized partial differential equations. The method is based on an Alternating-Direction-Predictor-Corrector (ADPC) scheme to solve the time-dependent Navier–Stokes equations. ADPC is a slight variation of Alternating-Direction-Implicit (ADI) method. It is first-order accurate in time but is effective and implemented easily when embedded in a large iteration scheme (Patnaik 1986; Patnaik *et al.* 1986). The control volume formulation is used to develop the finite-difference equations from the governing equations with respect to the generalized coordinates (ξ, η, ζ). One of the advantages of the control volume formulation is that mass and momentum are conserved over a single control volume, and hence the whole domain regardless of the grid fineness. An important part of solving the Navier–Stokes equations in primitive variables is the calculation of the pressure field. In the present work, a pressure correction equation is employed to satisfy indirectly the continuity equation (Anderson, Tannehill & Pletcher 1984). The pressure correction equation is of the Poisson type and is solved by the Successive-Over-Relaxation (SOR) method.

The overall solution procedure is based on a cyclic series of guess-and-correct operations. The velocity components are first calculated from the momentum equations using the ADPC method, where the pressure field at the previous timestep is employed. This estimate improves as the overall iteration continues. The pressure correction is calculated from the pressure correction equation using the SOR method, and new estimates for pressure and velocities are obtained. This process continues until the solution converges at each time-step.

$N_1 \times N_2 \times N_3$	C_{DP}	C_{DV}	C_D	C_D^*
		$Re = 20$		
$21 \times 21 \times 21$	1.048	1.777	2.825	
$31 \times 31 \times 31$	1.039	1.740	2.779	
$41 \times 41 \times 41$	1.037	1.731	2.768	2.74
		$Re = 100$		
$21 \times 21 \times 21$	0.560	0.590	1.150	
$31 \times 31 \times 31$	0.535	0.582	1.117	
$41 \times 41 \times 41$	0.526	0.581	1.107	1.09

TABLE 1. Drag coefficients as a function of grid density at $Re = 20$ and 100, where * denotes the data from the correlation of Clift *et al.* (1978).

3. Results and discussion

In §(3.1), we test the accuracy of the full three-dimensional solution procedure by predicting the axisymmetric flow over a single sphere and by examining the effects of grid resolution on the maximum lift coefficient of the sphere owing to the interaction between a vortex tube and a sphere. In §§(3.2), (3.3), (3.4) and (3.5), we discuss the three-dimensional interactions between a vortex tube and a sphere, the effects of the offset distance, the size of the vortex tube, and Reynolds number, respectively.

3.1. *Numerical accuracy*

Here we examine the flow generated by an impulsively started solid sphere in a quiescent fluid at two Reynolds numbers: 20 and 100. The time-dependent solution converges asymptotically to a steady-state which is in good agreement with the available experimental data and correlations as shown in tables 1 and 2. Table 1 lists the drag coefficients as a function of the computational grid density at Reynolds numbers 20 and 100, respectively, and compares them with the correlations of Clift, Grace and Weber (1978). Table 2 shows the pressures at the front and rear stagnation points and the separation angle measured from the front stagnation point as a function of grid density at Reynolds number 20 and 100, in comparison with the data of Taneda (1956) and also with the correlations of Clift *et al.* (1978). Although the solutions in these test cases are axisymmetric, none of the three velocity components in our formulation becomes identically zero. Therefore, the three-dimensional solution scheme is fully exercised here. The calculations were performed for three different grids, $(N_1 \times N_2 \times N_3) = (21 \times 21 \times 21)$, $(31 \times 31 \times 31)$ and $(41 \times 41 \times 41)$, in a computational domain with an outer boundary located at 21 sphere radii from the sphere centre.

We tested the solution procedure by varying the far-field boundary condition and by changing the location of the outer boundary. In the first test, the far-field outflow boundary condition was changed from $\partial\phi/\partial r = 0$ to $\partial\phi/\partial z = 0$ ($\phi = u$, v or w). There was almost no difference in the drag coefficient and the near wake size (the separation angle and length of the recirculation eddy) at Reynolds numbers 20 and 100. Our calculation shows that separation does not occur at Reynolds number 20. In the second test, the location of the outer boundary in downstream was changed from 21 to 41 sphere radii. There was virtually no change in the drag coefficient and the near wake size at both Reynolds numbers.

We examined the effects of grid resolution on the lift coefficients of the sphere owing to the flow interaction between a cylindrical vortex tube flowing with the free stream

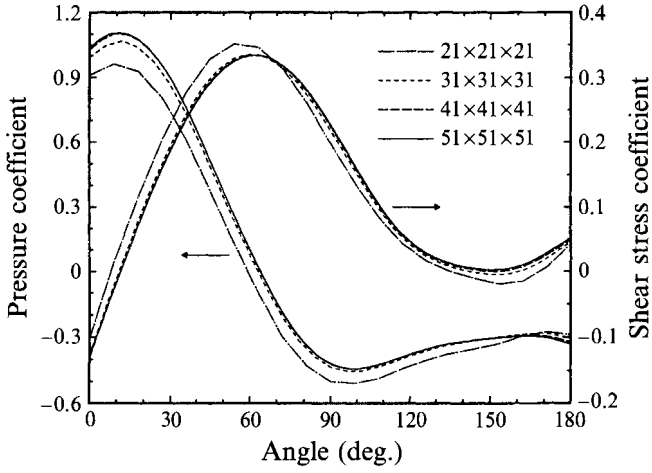

FIGURE 4. Pressure and shear stress distributions around the sphere in the (x, z)-plane of symmetry as a function of grid resolution at $t = 12$ for $Re = 100$, $d_{off} = 0$, $\sigma = 1$, and $v_{max} = 0.4$.

$N_1 \times N_2 \times N_3$	P_{of}	P_{or}	θ_s	θ_s^*
		$Re = 20$		
$21 \times 21 \times 21$	0.668	−0.201	180	
$31 \times 31 \times 31$	0.707	−0.178	180	
$41 \times 41 \times 41$	0.721	−0.171	180	180
		$Re = 100$		
$21 \times 21 \times 21$	0.554	−0.093 8	124.09	
$31 \times 31 \times 31$	0.554	−0.083 1	125.62	
$41 \times 41 \times 41$	0.554	−0.079 2	126.16	126.5

TABLE 2. Pressure at the front and rear stagnation points and the separation angle measured from the front stagnation point as a function of grid density at $Re = 20$ and 100, where * denotes the data from Taneda (1956) and the correlation of Clift *et al.* (1978).

$N_1 \times N_2 \times N_3$	$C_{L,max2,p}$	$C_{L,max2,v}$	$C_{L,max2}$
	$Re = 20$		
$21 \times 21 \times 21$	−0.336	−0.359	−0.695
$31 \times 31 \times 31$	−0.358	−0.363	−0.722
$41 \times 41 \times 41$	−0.362	−0.363	−0.725
	$Re = 100$		
$21 \times 21 \times 21$	−0.336	−0.159	−0.495
$31 \times 31 \times 31$	−0.433	−0.186	−0.619
$41 \times 41 \times 41$	−0.476	−0.192	−0.668
$51 \times 51 \times 51$	−0.494	−0.191	−0.685

TABLE 3. Maximum negative lift coefficients as a function of grid density at $Re = 20$ and 100.

and a sphere fixed in space at Reynolds numbers 20 and 100. The lift coefficients are obtained for the offset distance $d_{off} = 0$, vortex core radius $\sigma = 1$, and maximum fluctuation velocity $v_{max} = \Gamma_v/(2\pi\sigma) = 0.4$. Table 3 shows the maximum negative lift coefficient (C_{Lmax2}) of the sphere as a function of the computational grid density at

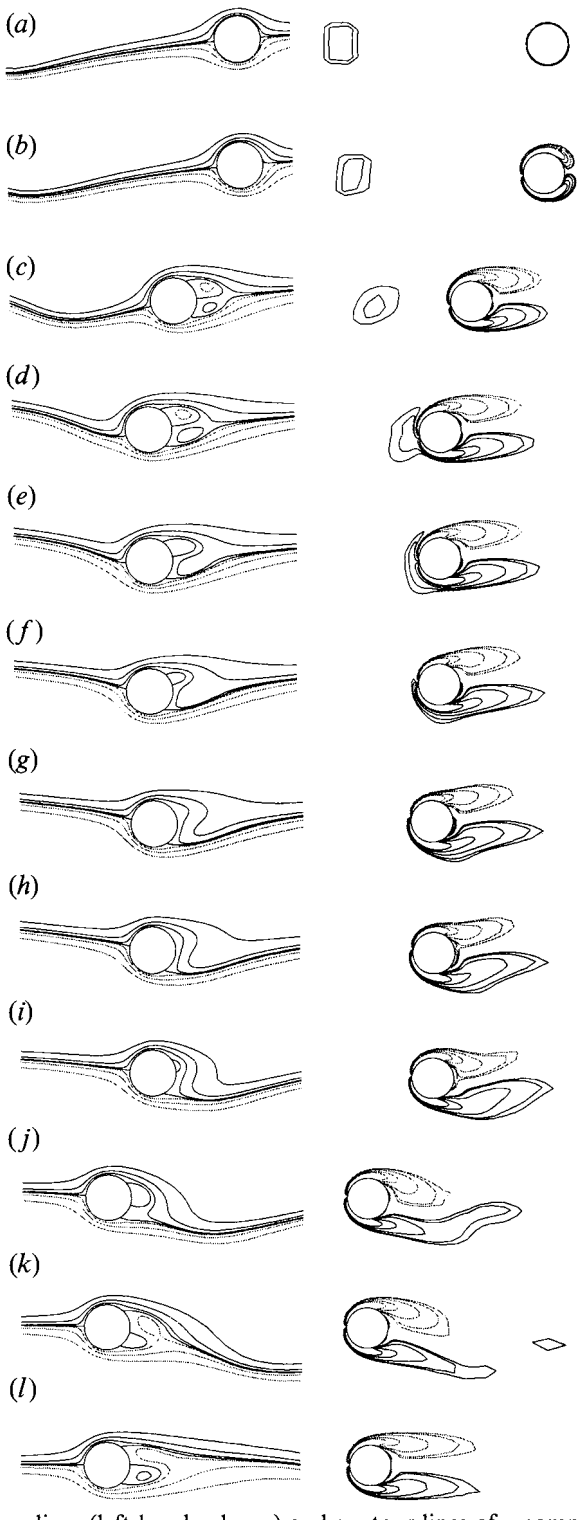

FIGURE 5. Pseudo-streamlines (left-hand column) and contour lines of y-component vorticity (right-hand column) in the principal plane at (*a*) $t = 0$, (*b*) 1, (*c*) 6, (*d*) 9, (*e*) 10, (*f*) 11, (*g*) 12, (*h*) 13, (*i*) 15, (*j*) 18, (*k*) 21 and (*l*) 30 for $Re = 100$, $d_{off} = 0$, $\sigma = 1$ and $v_{max} = 0.4$.

Reynolds numbers 20 and 100. The calculations were performed for three different grids, $(N_1 \times N_2 \times N_3) = (21 \times 21 \times 21)$, $(31 \times 31 \times 31)$ and $(41 \times 41 \times 41)$ for $Re = 20$, and four different grids, $(N_1 \times N_2 \times N_3) = (21 \times 21 \times 21)$, $(31 \times 31 \times 31)$, $(41 \times 41 \times 41)$ and $(51 \times 51 \times 51)$ for $Re = 100$, in a computational domain with an outer boundary located at 21 sphere radii from the sphere centre. The result of the $31 \times 31 \times 31$ grid differs by 0.42% for that of the $41 \times 41 \times 41$ grid for $Re = 20$, and the result of the $41 \times 41 \times 41$ grid differs by 2.5% from that of the $51 \times 51 \times 51$ grid for $Re = 100$. Figure 4 provides additional results on the effect of grid resolution on convergence and shows the distributions of the pressure and shear stress coefficients (normalized by the dynamic pressure) around the sphere in the (x, z)-plane of symmetry in the positive x-direction for the same parameters as used above with $Re = 100$. The pressure and shear stress distributions were obtained at $t = 12$ about which the lift coefficient reaches its maximum in negative value. The pressure coefficient at $(x, z) = (0, -1)$ of the $41 \times 41 \times 41$ grid differs by 0.93% from that of the $51 \times 51 \times 51$ grid. The same calculations were performed by changing the location of the outer boundary in downstream from 21 to 41 sphere radii. There was virtually no change in the lift, moment and drag coefficients.

In order to examine the far-field boundary effects, we repeated the simulation as above for $Re = 100$, $d_{off} = 0$, $\sigma = 1$, and $v_{max} = 0.4$ but with a box-type computational domain with symmetry boundary conditions on its sides. The lift, moment and drag coefficients of the box-type computational domain at $t = 12$ differs by 0.12%, 0.17% and 0.13%, respectively, from those of the spherical computational domain used in the present paper. The spherical computational domain gives a little finer resolution than does the box-type computational domain with the same number of grid points, and so smoother contour lines for the vorticity and stream lines in the (x, y) symmetry plane. We also solved the same problem as above by employing a complete computational domain without the symmetry plane and periodic boundary condition in the ζ-direction. In that case, the lift coefficients differ by 0.16% from those in table 3 where the symmetry condition was employed. The $41 \times 41 \times 41$ grid is used in the following calculations.

The run for the interaction between a vortex tube and a sphere at Reynolds number 100 with the $41 \times 41 \times 41$ grid required 2.62 mega words, a dimensionless timestep of $\Delta t = 0.0025$, and a total time of 2.95 c.p.u. hours on Cray Y-MP8/864 for the final time of $t_f = 24$. Each timestep takes about 1.11 c.p.u. seconds. Another test was performed to examine the effects of the timestep. The same calculation as above was repeated for $Re = 100$, $d_{off} = 0$, $\sigma = 1$, and $v_{max} = 0.4$ but with the time-step reduced by half. The lift, moment and drag coefficients differ by 0.25%, 0.19% and 0.003%, respectively, from those obtained with the timestep used in the presented results.

3.2. *Interactions of a vortex tube and a sphere*

We consider the interactions of a vortical structure advected by the free stream and a sphere suddenly placed in the flow and held fixed in space at Reynolds number 100. The vortical structure is initially a cylindrical vortex tube rotating counter-clockwise in figure 1 with a non-dimensional radius of unity and an offset distance of zero, and located at 10 sphere-radii upstream from the centre of the sphere.

3.2.1. *Flow structure*

In order to illustrate better the fluid motion, we consider the flow field in the (x, z)-plane of symmetry, which is defined as the principal plane, where the strongest interactions occur between the vortical structure and the sphere.

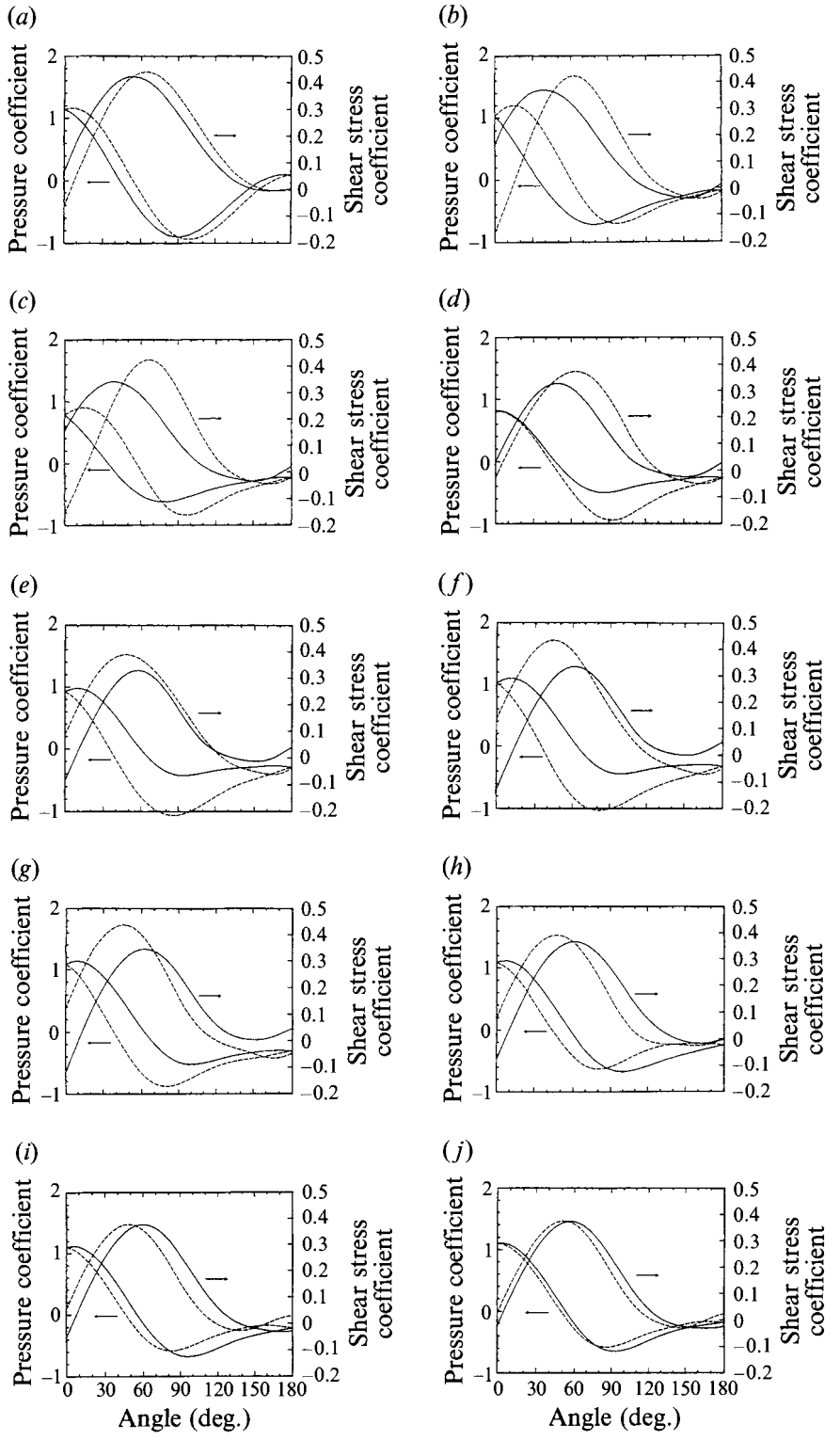

FIGURE 6. Pressure and shear stress distributions around the sphere in the principal plane at (*a*) $t = 1$, (*b*) 6, (*c*) 9, (*d*) 10, (*e*) 11, (*f*) 12, (*g*) 13, (*h*) 15, (*i*) 18 and (*j*) 21 for $Re = 100$, $d_{off} = 0$, $\sigma = 1$ and $v_{max} = 0.4$. ——, upper; – – –, lower.

Pseudo-streamlines are employed in the following illustrations. The pseudo-streamlines are obtained from the pseudo-stream function which is defined by assuming that the velocity field in the principal plane does not change in the perpendicular direction to the principal plane and by using the two-dimensional stream function definition. The sphere surface in the principal plane is used as a reference streamline ($\psi_{ps} = 0$). We note that a real stream function ψ cannot be defined and calculated from the velocity in the principal plane owing to the existence of a divergence associated with the third component of velocity. Nevertheless, for descriptive purposes only, it is convenient to use the two-dimensional stream function definition to present approximations to the streamline pattern.

Figures 5(*a*)–5(*l*) display the pseudo-streamlines (left-hand column) and the contour lines of y-component vorticity (right-hand column) in the principal plane at $t = 0$, 1, 6, 9, 10, 11, 12, 13, 15, 18, 21 and 30 for $Re = 100$, $d_{off} = 0$, $\sigma = 1$, and $v_{max} = \Gamma_v/(2\pi\sigma) = 0.4$. The contour values of the pseudo-streamlines are 0, ± 0.02, ± 0.1 and ± 0.3. The contour values of the vorticity are ± 0.4, ± 0.5, ± 0.8, ± 1.4 and ± 2, with the highest magnitude at the sphere surface. The solid and dotted lines in the figures represent positive and negative values. Figures 6(*a*)–6(*j*) show the pressure coefficient, $2(p-p_\infty)/\rho U_\infty^2$, and shear stress coefficient, $2\tau_{r\theta}/\rho U_\infty^2$, around the sphere in the principal plane, respectively, at $t = 1$, 6, 9, 10, 11, 12, 13, 15, 18 and 21. Note that figure 6(*a*) is for $t = 1$ which corresponds to figure 5(*b*).

At $t = 0$, figure 5(*a*) shows that a spherical vortex sheet is generated around the sphere owing to the no-slip condition at the sphere surface. The subsequent figures show that the vortex sheet around the sphere is advected downstream as well as diffused outwards from the sphere. The vorticity on the edge of the vortex core is 0.4 at $t = 0$ for $\Gamma_v = 2.51$ and $\sigma = 1$ which correspond to $v_{max} = \Gamma_v/(2\pi\sigma) = 0.4$. The vortex tube is initially cylindrical and thus should appear as a circle in the principal plane. However, the vortex tube in figure 5(*a*) is not an exact circle because the grid resolution is relatively coarse at the initial location of the vortex tube which is far upstream from the sphere and the linear interpolation is used to draw the contour lines. However, we calculate analytically the exact velocity and pressure fields induced by the vortex tube by using equations (1) and (2), and prescribe them as initial conditions. Therefore, the magnitudes of the initial velocity components at a given location (x, z) are fixed no matter what grid distribution is used. Thus, the circulation around a large circle enclosing the vortex tube remains the same as that of the vortex tube. The velocity and pressure fields as a function of time are almost not affected by the initial vortex tube shape obtained by the linear interpolation. The line connecting the front and rear stagnation points in the standard axisymmetric flow over a single sphere, which is the $x = 0$ line in the principal plane, will be used as a reference line. We refer to the region above the line as 'upper' region and that below the line as 'lower' region.

For $0 < t \leqslant 9$, the vortex tube is upstream of the sphere as shown in figures 5(*b*)–5(*d*). The vortex tube rotating counterclockwise produces downwash upstream of itself and upwash downstream. Therefore, the front stagnation point on the sphere is shifted below the plane $x = 0$ owing to the upwash, and thus, the fluid particles in the upper left-hand region move faster than do those in the lower left region of the sphere. As a consequence, lower pressure and higher shear stress act in the upper left-hand region compared to the lower left-hand region as shown in figures 6(*a*)–6(*c*), and this causes a positive lift force on the sphere. Note that in figure 6 the clockwise direction is considered positive for the shear stress in the upper region of the sphere, and the counterclockwise direction is considered positive for the shear stress in the lower

region. On the other hand, the shift of the front stagnation point below the plane $x = 0$ causes the fluid particles to continue to accelerate after $\theta = 90°$ at the bottom of the sphere but to begin to decelerate before $\theta = 90°$ at the top of the sphere where θ is measured from the negative z-axis, as shown in the pressure distribution around the sphere in the principal plane in figures 6(*a*)–6(*c*). Thus the fluid particles move faster in the bottom and lower right-hand regions than in the top and upper right-hand regions of the sphere. As a consequence, lower pressure and higher shear stress act in the bottom and lower right-hand regions compared to the top and upper right-hand regions as shown in figures 6(*a*)–6(*c*), and this causes the fluid particles turning around the upper eddy to be pushed into the lower region of the near wake as shown in figures 5(*c*) and 5(*d*). Figures 5(*c*) and 5(*d*) also show that the upper eddy is formed by the fluid separating on the upper portion of the sphere as in the case of axisymmetric flow past a sphere without the presence of the vortex tube. On the other hand, the lower eddy is not formed by the fluid separating on the lower portion of the sphere, but rather by the fluid turning around the upper eddy and being entrained by the lower flow. This lower eddy is detached from the sphere. A portion of the fluid moving around the top of the sphere passes between the detached lower eddy and the sphere. A similar flow pattern was found by Kim, Elghobashi & Sirignano (1993) in their study of three-dimensional flow over two spheres placed side by side.

For $9 < t \leqslant 10$, the figures 5(*d*) and 5(*e*) shows that the vortex tube contacts the boundary layer of the sphere.

For $10 < t \leqslant 13$, the figures 5(*f*)–5(*h*) show that the vortex tube goes around the bottom of the sphere. The vortex tube is now downstream of the front stagnation point in the axisymmetric flow past a sphere and produces downwash on the sphere. Therefore, the front stagnation point on the sphere is shifted above the plane $x = 0$, and thus the fluid particles in the lower left-hand region move faster than do those in the upper left-hand region of the sphere. As a consequence, lower pressure and higher shear stress act in the lower left-hand region compared to the upper left-hand region as shown in figures 6(*e*)–6(*g*), and this causes the negative lift force on the sphere. On the other hand, the shift of the front stagnation point above the plane $x = 0$ causes the fluid particles to move faster in the boundary layer of the top and upper right-hand regions compared to that of the bottom and lower right-hand regions of the sphere as shown in figure 7, which shows the tangential velocity profiles, $u_\theta(r)$, at $\theta = 90°$ on the top and the bottom of the sphere in the principal plane at $t = 12$, and this causes the higher shear stress in the top and upper right-hand regions compared to the bottom and lower right-hand regions as shown in the figures 6(*f*) and 6(*g*). However, during this time period, the pressure distributions at the top and bottom of the sphere in the principal plane have different features from those of the shear stress owing to the following reason. The counterclockwise vortex tube in the uniform stream produces a flow field in which the fluid velocity is less than that of the uniform stream above the vortex tube and higher than that of the uniform stream below the vortex tube with respect to fixed coordinate system in space. Owing to this shear flow, the fluid velocity on the edge of (and outside) the boundary layer at the bottom of the sphere is larger than that at the top of the sphere as shown in figure 7, and thus the pressure at the bottom of the sphere is lower than that at the top of the sphere. This pressure difference causes the fluid particles turning around the top of the sphere to be pushed into the lower region of the wake forming an S-shaped path (figures 5(*g*) and 5(*h*)). The combined effect of the upward shift of the front stagnation point owing to downwash of the vortex tube and the velocity difference between the top and the bottom of the sphere owing to the shear flow induced by the vortex tube results in a higher magnitude

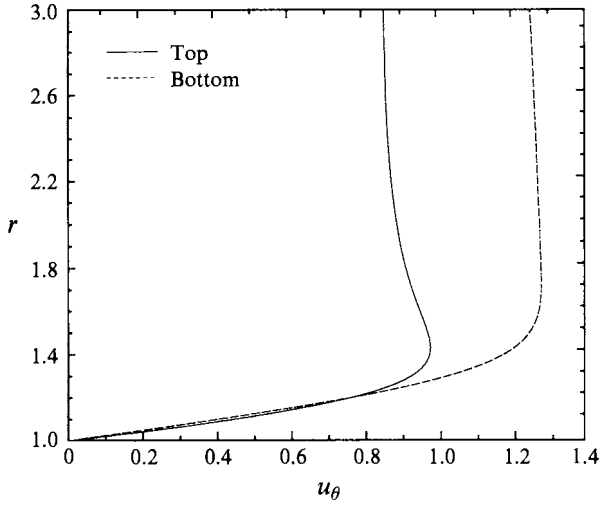

FIGURE 7. Tangential velocity profile, $u_\theta(r)$, at $\theta = 90°$ on the top and the bottom of the sphere in the principal plane at $t = 12$.

of the maximum negative force than that of the maximum positive force, as will be shown in detail in §3.2.2. The upper separation eddy becomes smaller during this time period, because the pressure difference between the upper and lower wake just downstream of the sphere becomes larger when the vortex tube passes the plane $z = 1$ (tangent to the rear stagnation point in axisymmetric flow), and more fluid particles are pushed into the lower wake just behind the sphere. At $t = 12$ and 13, no separation eddies appear in the wake as shown in figures 5(*g*) and 5(*h*), and the flow does not separate in the upper region of the sphere as shown in figures 5(*g*), 5(*h*), 6(*f*) and 6(*g*). We note that the separation point in the principal plane is the point at which the shear stress vanishes.

The reason for the passage of the counterclockwise-rotating vortex tube around the bottom of the sphere rather than around the top is as follows. First, note that the well-known two-dimensional, inviscid case of a vortex interacting with a cylinder has a counterclockwise (clockwise) rotating vortex advecting clockwise (counterclockwise) around the cylinder. In our case, the opposite behaviour suggests that viscosity is important in this phenomenon. Note further that the vorticity levels associated with the viscous boundary layer on the sphere are greater than those associated with the tube. When the counterclockwise-rotating vortex tube comes close to the sphere boundary layer, it augments the magnitude of the edge velocity in the lower boundary layer and reduces the edge velocity in the upper boundary layer. The result is a higher strength vorticity in the lower boundary layer than in the upper boundary layer (see the vorticity contours in figures 5(*d*)–5(*f*)). (The magnitude of the highest vorticity in the lower boundary layer is 15% higher than that in the upper boundary layer at $t = 9$.) Consequently, the vorticity in the lower boundary layer induces a velocity in the downward direction at the location of the vortex tube with higher magnitude than that induced by the vorticity in the upper boundary layer. This downward induced velocity advects the vortex tube below the sphere.

For $13 < t \leqslant 19$, the vortex tube is downstream of the sphere as shown in figures 5(*i*) and 5(*j*) and produces downwash on the sphere. Therefore, the negative lift force acts on the sphere owing to the shift of the front stagnation point above the plane $x = 0$ in

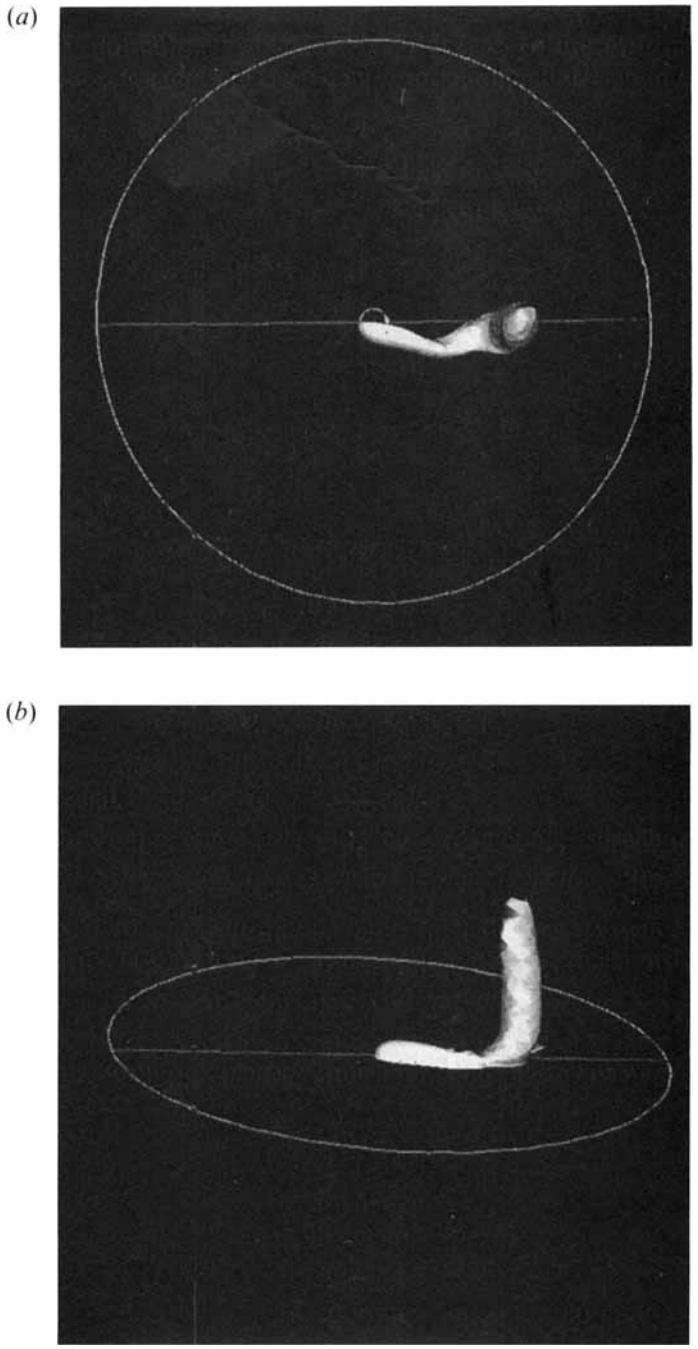

FIGURE 8. Two views of a three-dimensional contour surface of $\omega_y = 0.2$ at $t = 20$ for the flow depicted in figure 5; (*a*) a side view looking normal to the principal plane (*b*) a view looking down with an acute angle toward the (y, z)-plane.

a similar manner as for $10 < t \leqslant 13$, but the negative lift force is reduced as the vortex tube moves further downstream. The shift of the front stagnation point above the plane $x = 0$ causes the fluid particles to move faster in the top and upper right-hand regions than in the bottom and lower right-hand regions of the sphere, and this causes

the lower pressure and higher shear stress in the top and upper right-hand regions compared to those in the bottom and lower right-hand regions as shown in figures 6(*h*) and 6(*i*). However, because the vortex tube is still intersecting the near wake and thus producing strong downwash in the near wake, the fluid particles turning around the top of the sphere are pushed into the lower region of the near wake. This allows no room for the lower eddy to grow. On the other hand, the upper eddy grows as the vortex tube moves downstream because the fluid particles turning around the top of the sphere experience less force pushing them into the lower region of the near wake.

For $t \geqslant 20$, the vortex tube is far downstream of the sphere as shown in figures 5(*k*) and 5(*l*) and produces weak downwash on the sphere, and thus the lift force on the sphere is almost zero as will be shown in §3.2.2. The weak downwash causes the front stagnation point on the sphere to be shifted slightly above the plane $x = 0$, and thus the fluid particles move slightly faster in the top and upper right-hand regions than in the bottom and lower right-hand regions of the sphere, and this causes the higher shear stress and lower pressure in the top and upper right-hand regions as shown in figure 6(*j*). Now, the downward force due to the vortex tube is very weak in the near wake because the vortex tube is far downstream. Therefore, the lower eddy grows, and owing to the lower pressure in the upper region of the sphere, the fluid particles turning around the lower eddy are pushed up into the upper near wake as shown in figures 5(*k*) and 5(*l*).

We now examine a three-dimensional view of the vortex tube by considering the y-component of vorticity vector. Figures 8(*a*) and 8(*b*) show two views of a three-dimensional contour surface of $\omega_y = 0.2$ at $t = 20$ for the flow depicted in figure 5. Figure 8(*a*) shows a side view looking normal to the principal plane, whereas figure 8(*b*) shows a view looking down with an acute angle toward the (y, z)-plane. The ellipse in figure 8(*b*) is the boundary of the spherical computational domain viewed at an angle. It appears as a circle when viewed normal to the principal plane. The sphere is at the centre of the domain in figures 8(*a*) and 8(*b*). Figure 8(*b*) shows that the portion of the vortex tube in the principal plane is retarded, owing to its interaction with the sphere, compared with the rest of the vortex tube (in the (y, z)-plane with its axis parallel to the y-axis) outside the principal plane. By measuring the radial extent of the contour surface (of $\omega_y = 0.2$ at $t = 20$) in figures 8(*a*) and 8(*b*), we find that the maximum radius of the contour surface outside the principal plane is 1.58 which is very close to the value of 1.6 taken from figure 3(*b*).

3.2.2. *Lift, moment, and drag coefficients and effect of tube circulation*

Figure 9 shows the lift coefficients of the sphere as a function of time for $Re = 100$, $d_{off} = 0$, and $\sigma = 1$. The lift coefficients are computed for four different maximum fluctuation velocities ($v_{max} = \Gamma_v/(2\pi\sigma)$) due to the vortex tube, with magnitudes equal to 0.1, 0.2, 0.3 and 0.4 (normalized by free-stream velocity). Owing to the sudden placement of the sphere into the stream, it initially takes a small time ($0 < t < 0.6$) for the initial flow perturbations to vanish.

As discussed earlier, when the vortex tube approaches the sphere ($0 \leqslant t \leqslant 9.4$), it produces upwash resulting in a positive lift force on the sphere. The maximum positive lift coefficient $C_{L,max1}$ occurs at $t = 7.2$. On the other hand, when the vortex tube passes the sphere, it produces downwash and high fluid velocity near the bottom of the sphere resulting in a negative lift force. The magnitude of the negative lift is greater than the positive lift (figure 9). The maximum negative lift coefficient $C_{L,max2}$ occurs at $t = 11.8$ about when the centre of the vortex tube passes the plane $z = 1$. The lift coefficient is linearly proportional to the maximum fluctuation velocity (or the

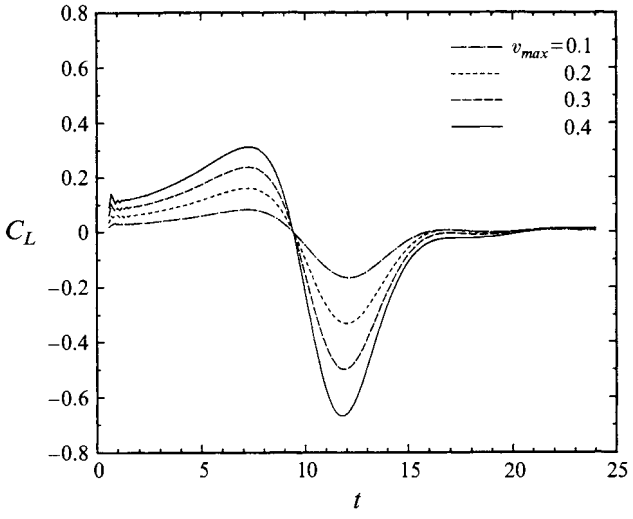

FIGURE 9. Lift coefficients of the sphere as a function of time and v_{max} for $Re = 100$, $d_{off} = 0$ and $\sigma = 1$.

circulation of the vortex tube for constant vortex core radius) until the vortex tube contacts the sphere boundary layer ($t \leqslant 9.4$). The maximum positive lift coefficient $C_{L,max1}$ is expressed by

$$C_{L,max1} = cv_{max}, \tag{18}$$

where the proportionality constant $c = 0.8$. For $t > 9.4$, the relation between the lift coefficient and v_{max} deviates slightly from linearity, but the maximum negative lift coefficient $C_{L,max2}$ is linearly proportional to v_{max} with $c = -1.66$. After the lift coefficient reaches its maximum negative value, it decays quickly towards zero because the vortex tube vorticity is diffused in the sphere wake. The time averaged lift coefficient (averaged over a time span between $t = 0.6$ and the maximum time 24) for all values of v_{max} is small and negative ($O(10^{-2})$). As mentioned earlier, the behaviour of $C_L(t)$ during the period $0 < t < 0.6$ is influenced by the initial flow perturbation, and thus its value during this initial period is excluded from the averaging process. The root mean square $C_{L,rms}$ of the lift coefficient as a function of time is also linearly proportional to v_{max} with $c = 0.65$ as will be shown in table 4.

Figure 10 shows the temporal development of the moment coefficients for the sphere under the same conditions as figure 9. The moment coefficients are obtained for four different values of $v_{max} = 0.1$, 0.2, 0.3 and 0.4.

As the vortex tube approaches the sphere, the downward shift of the front stagnation point (due to the upwash) causes higher shear stress in the upper left-hand region compared to the lower left-hand region generating a negative (clockwise) torque. At the same time, the downward shift causes higher shear stress in the bottom and lower right-hand regions compared to the top and upper right-hand regions as explained in §3.2.1 generating a positive torque. The two torques compete with each other and result in a net weak torque in the interval $0 < t \leqslant 9$.

As the vortex tube passes the sphere ($9 < t \leqslant 14$), the upward shift of the front stagnation point (due to the downwash) causes higher shear stress in the lower left-hand region compared to the upper left-hand region generating a positive torque. At the same time, the upward shift caused higher shear stress in the top and upper right-

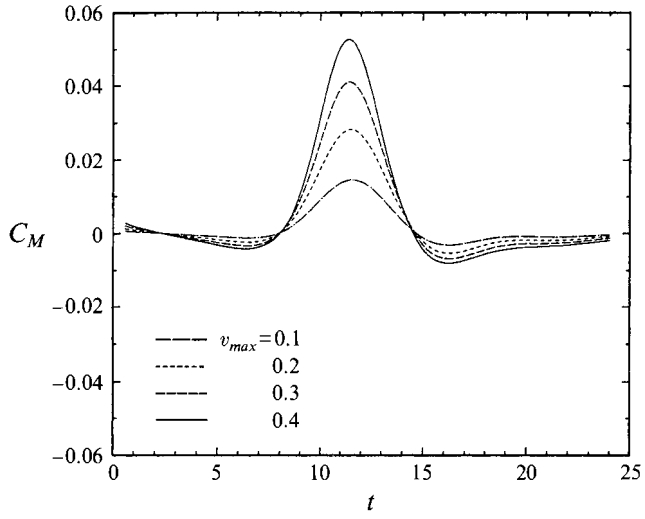

FIGURE 10. Moment coefficients of the sphere under the same conditions as figure 9.

hand regions compared to the bottom and lower right-hand regions as explained in §3.2.1 generating a negative torque. However, the effect of this negative torque is diminished by the shear flow induced by the vortex across the sphere which produces high shear stress at the bottom of the sphere. As a consequence, a net high positive torque acts on the sphere. The maximum positive moment coefficient $C_{M,max}$ occurs at $t = 11.4$. $C_{M,max}$ is linearly proportional to v_{max} with a proportionality constant $c = 0.14$.

When the vortex tube is relatively far downstream from the sphere ($t > 15$), the positive torque due to the shear stress in the lower left-hand region competes with the negative torque due to the shear stress in the top and upper right-hand regions. This results in a net weak negative torque which becomes smaller as the vortex tube moves farther downstream. We note that the torque depends only on the distribution of the shear stresses and is relatively small compared to the lift force.

The time-averaged moment coefficient (averaged over a time span between $t = 0.6$ and 24) for all values of v_{max} is nearly zero ($O(10^{-3})$), and the root mean square $C_{M,rms}$ of the moment coefficient is approximately linearly proportional to v_{max} with $c = 0.05$.

Figure 11 shows the drag coefficients of the sphere as a function of time for the same conditions as figure 9. The drag coefficients are computed for four different values of $v_{max} = 0.1$, 0.2, 0.3 and 0.4.

As discussed earlier, the sudden placement of the sphere in the flow results in initially large values of shear stress and pressure on the sphere, and hence a large drag as shown in figure 11. Figure 5(*e*) shows that at about $t = 10$ the centre of the vortex tube is located near the front stagnation point which is slightly below the point $(x, y, z) = (0, 0, -1)$. Owing to the low pressure at the centre of the vortex tube, the pressure coefficient at the front stagnation point ($C_{po} = 0.818$) is lower than that of the axisymmetric flow past a sphere without the vortex tube ($C_{po,axi} = 1.107$) as shown in figure 6(*d*). Also, the maximum shear stresses in the upper and lower regions are lower than that of the axisymmetric flow without the vortex tube. This causes the drag on the sphere to be lower than that of the axisymmetric flow without the vortex tube. As the vortex tube moves around the bottom of the sphere, the front stagnation point is

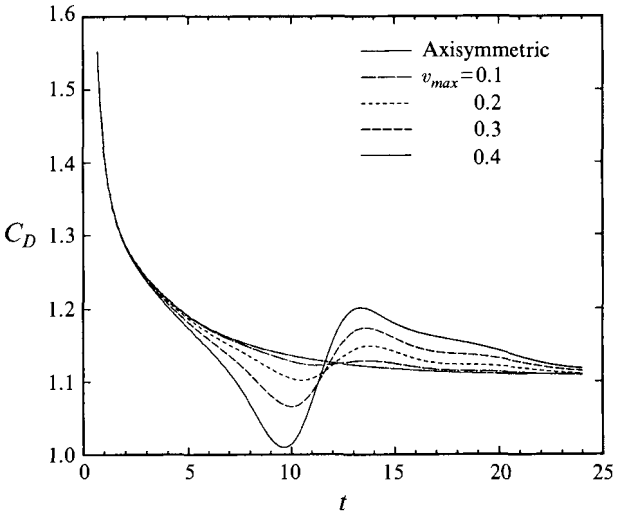

FIGURE 11. Drag coefficients of the sphere under the same conditions as figure 9.

shifted above the plane $x = 0$, owing to the downwash. Consequently, high pressure and higher shear stress act in the upper and lower left-hand regions, respectively, as explained earlier in §3.2.1. This increases the drag during the periods $10 < t \leqslant 13.4$. For $t > 13.4$, the drag approaches that of the axisymmetric flow as the vortex tube moves further downstream.

The time-averaged value of the deviation of the drag coefficient from that of the axisymmetric flow past a sphere for all values of v_{max} is nearly zero ($O(10^{-4})$). The unsteady drag coefficient of the axisymmetric flow past a sphere was computed for a sphere suddenly placed in the uniform stream without the vortex tube.

3.3. *Effects of the offset distance*

We examine the effects of the offset distance on the flow field by varying d_{off} while using the same flow conditions as in §3.2.

3.3.1. *Offset distance* $1 \leqslant d_{off} \leqslant 4$

The temporal behaviours of the lift and moment coefficients of the sphere for $d_{off} = 1$ are similar to those in the case of $d_{off} = 0$. The main feature distinguishing the case of $d_{off} = 1$ from that of $d_{off} = 0$ is that in the former, the vortex tube splits into two parts when the vortex tube passes the sphere. The attraction of the vortex tube to the positive vorticity in the boundary layer at the bottom of the sphere causes some portion of the vortex tube to move around the bottom of the sphere, whereas the other portion moves on the top of the sphere, as shown in figure 12. Figures 12(*a*)–12(*h*) display the contour lines of y-component vorticity in the principal plane at $t = 9$, 10, 11, 12, 13, 15, 18 and 21 for $Re = 100$, $d_{off} = 1$, $\sigma = 1$, and $v_{max} = 0.4$. The contour values of the vorticity are ± 0.4, ± 0.5, ± 0.8, ± 1.4 and ± 2. Owing to its longer interaction with the sphere for $d_{off} = 1$ than for $d_{off} = 0$, the magnitudes of the lift and moment coefficients of the sphere are close to those in the case of $d_{off} = 0$ despite its positive offset distance initially. Equation (18) is approximately valid for $C_{L,max1}$, $C_{L,max2}$, $C_{L,rms}$, $C_{M,max}$, and $C_{M,rms}$ with the same proportionality constants as in the case of $d_{off} = 0$.

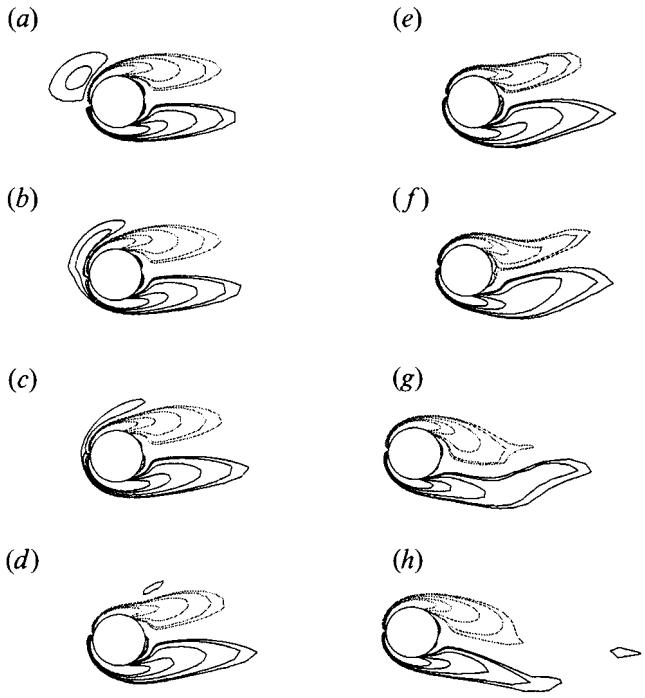

FIGURE 12. Contour lines of y-component vorticity in the principal plane at (*a*) $t = 9$, (*b*) 10, (*c*) 11, (*d*) 12, (*e*) 13, (*f*) 15, (*g*) 18 and (*h*) 21 for $Re = 100$, $d_{off} = 1$, $\sigma = 1$ and $v_{max} = 0.4$.

Figure 13(*a*) shows the drag coefficients of the sphere as a function of time for $Re = 100$, $d_{off} = 1$, and $\sigma = 1$. The drag coefficients are obtained with two different maximum fluctuation velocities due to the vortex tube, $v_{max} = 0.1$ and 0.2. The temporal behaviour of the drag coefficients is different from that of the case of $d_{off} = 0$. The time-averaged value of the deviation of the drag coefficient from that of the axisymmetric flow past a sphere for all values of v_{max} is not nearly zero but increases linearly as v_{max} increases. The time-averaged drag coefficient $C_{D,ave}$ is expressed by

$$C_{D,ave} = C_{D,axi} + \beta v_{max}, \tag{19}$$

where the constant $\beta = 0.2$, and $C_{D,axi}$ is the time-averaged value of the drag coefficient in the case of axisymmetric flow ($v_{max} = 0$). The drag coefficients reach their maximum at about $t = 10$. The maximum drag coefficient $C_{D,max}$ is expressed also by (19) but with $\beta = 0.62$, and $C_{D,axi}$ here is the local value of the axisymmetric drag coefficient at the time of $C_{D,max}$. At about $t = 10$, the centre of the vortex tube is located above the front stagnation point. Thus, the induced velocity due to the vortex tube adds its magnitude to the base flow along the stagnation streamline, and so the dynamic pressure ahead of the front stagnation point becomes higher than that of the axisymmetric flow past a sphere. This causes the pressure at the stagnation point and the shear stresses in the upper and lower left-hand regions to be higher than those of the axisymmetric flow past a sphere. As a consequence, the drag is increased. When the offset distance is negative, the reverse phenomena would occur, and the drag would be decreased. This will be discussed in §3.3.2.

Figures 14(*a*) and 14(*b*) display the contour lines of y-component vorticity in the principal plane at $t = 9$ and 12 for $Re = 100$, $d_{off} = 2$, $\sigma = 1$, and $v_{max} = 0.4$. The contour values of vorticities are the same as those of previous sections. Figures 14(*a*) and

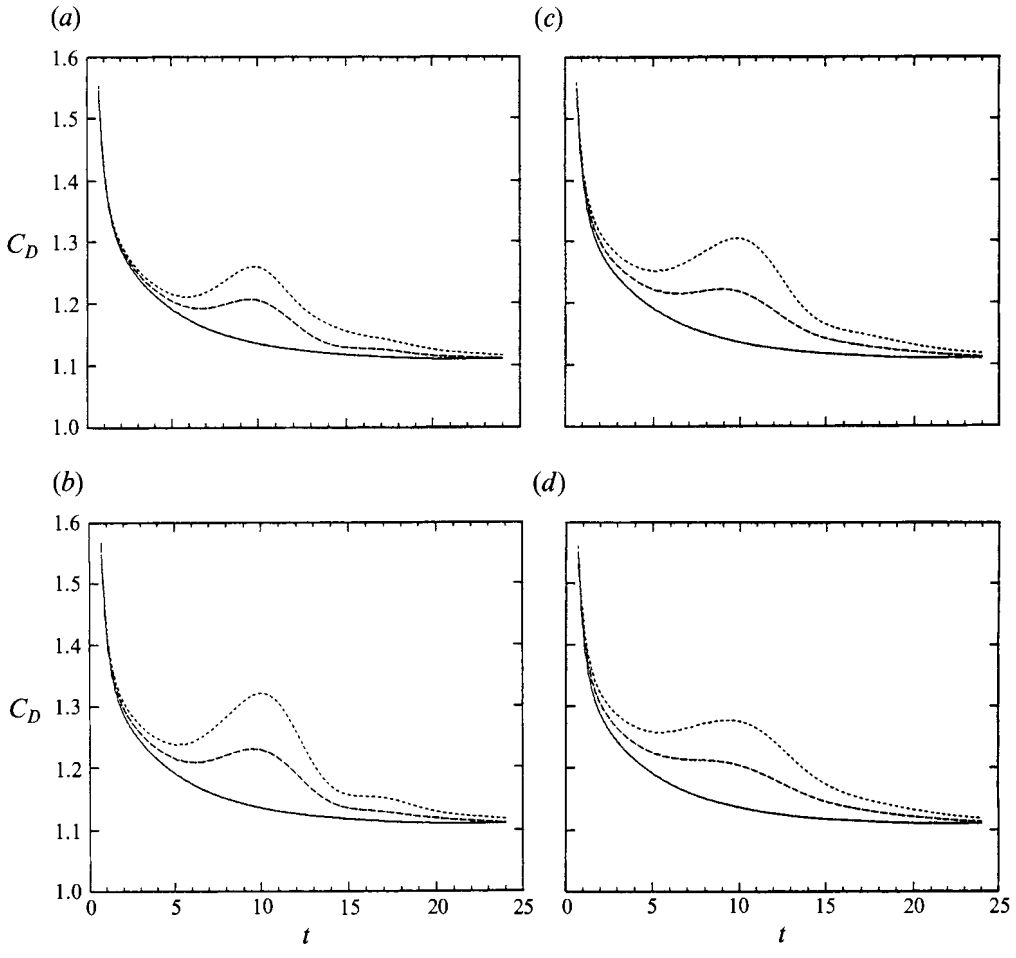

FIGURE 13. Drag coefficients of the sphere as a function of time and v_{max} for (*a*) $d_{off} = 1$, (*b*) 2, (*c*) 3 and (*d*) 4 with $Re = 100$ and $\sigma = 1$. ——, axisymmetric; – – –, $v_{max} = 0.1$; · · · ·, $v_{max} = 0.2$.

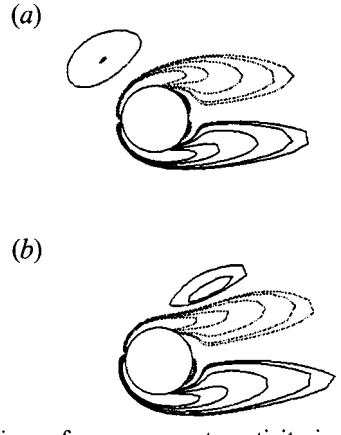

FIGURE 14. Contour lines of y-component vorticity in the principal plane at (*a*) $t = 9$ and (*b*) 12 for $Re = 100$, $d_{off} = 2$, $\sigma = 1$ and $v_{max} = 0.4$.

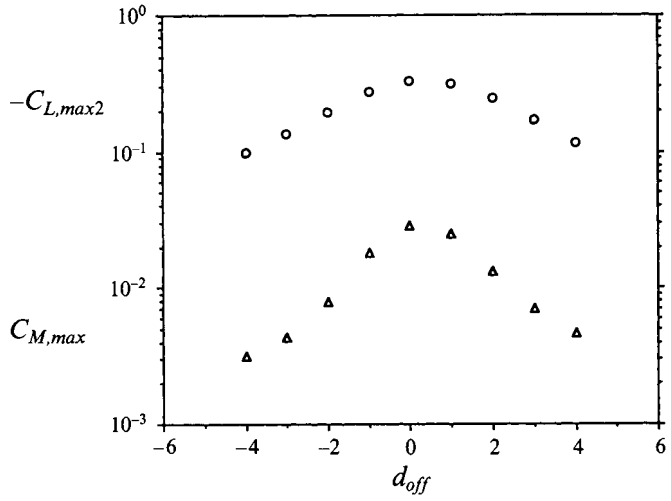

FIGURE 15. Magnitude of $C_{L,max2}$ and $C_{M,max}$ as a function of d_{off} for $Re = 100$, $\sigma = 1$ and $v_{max} = 0.2$.

14(*b*) show that the vortex tube passes above the sphere. The behaviour of the lift coefficients with time for $d_{off} = 2$, 3 and 4 is similar to that of the case of $d_{off} = 0$ and 1. However, their magnitudes are smaller than those for $d_{off} = 0$ and 1 and decay with d_{off} exponentially as shown in figure 15, where the magnitude of the negative maximum lift coefficient and the maximum moment coefficient for $Re = 100$, $\sigma = 1$, and $v_{max} = 0.2$ are presented as a function of d_{off}. The positive maximum lift coefficient $C_{L,max1}$ for $d_{off} \geqslant 2$ is expressed by

$$C_{L,max1} = c_1 v_{max} \exp(c_2 |d_{off}|), \tag{20}$$

where $c_1 = 0.99$ and $c_2 = -0.3$. The negative maximum lift coefficient $C_{L,max2}$ is expressed by (20) with $c_1 = -2.64$ and $c_2 = -0.38$, and the r.m.s. lift coefficient $C_{L,rms}$ is expressed also by (20) with $c_1 = 0.88$ and $c_2 = -0.28$.

The behaviour of the moment coefficients with time for $d_{off} = 2, 3$ and 4 is also similar to that of the case of $d_{off} = 0$ and 1. However, their magnitudes are smaller than those for $d_{off} = 0$ and 1 and decay with a negative power of d_{off} as shown in figure 15. The maximum moment coefficient $C_{M,max}$ for $d_{off} \geqslant 2$ is expressed by

$$C_{M,max} = c_3 v_{max} |d_{off}|^m, \tag{21}$$

where $c_3 = 0.185$ and $m = -1.501$. The r.m.s. moment coefficient $C_{M,rms}$ is expressed by (21) with $c_3 = 0.056$ and $m = -1.185$.

Figures 13(*b*), 13(*c*) and 13(*d*) show the drag coefficients of the sphere as a function of time for $d_{off} = 2$, 3 and 4, respectively, with $Re = 100$ and $\sigma = 1$. The drag coefficients are obtained with two different maximum fluctuation velocities due to the vortex tube, $v_{max} = 0.1$ and 0.2. The drag coefficients reach their maximum at about $t = 10$. The maximum drag coefficient $C_{D,max}$ for $d_{off} = 2$ is higher than that for $d_{off} = 1$ because the magnitude of the induced velocity added to the base flow along the stagnation streamline for $d_{off} = 2$ is higher than that for $d_{off} = 1$. We note that the radius of the vortex core is greater than unity at $t = 10$ owing to the diffusion (and the maximum induced velocity occurs at the edge of the vortex core) as shown in figure 3(*a*)

for $Re = 100$, $\sigma = 1$, and $v_{max} = 0.4$. $C_{D,max}$ decreases as d_{off} increases above 2. $C_{D,max}$ for $d_{off} = 2, 3$ and 4 are expressed by (19) with $\beta = 0.9$, 0.8 and 0.68, respectively. $C_{D,ave}$ for $d_{off} = 2, 3$ and 4 are expressed also by (19) with $\beta = 0.31$, 0.33 and 0.32, respectively. We note that the magnitude of the deviation of the drag coefficient from that of the axisymmetric flow decays slowly with d_{off}, in contrast with fast decay of the lift and moment coefficients with d_{off}.

3.3.2. *Offset distance* $-1 \geqslant d_{off} \geqslant -4$

Note that the sign reversal of the initial tube vorticity with the offset distance kept positive is a mirror image of the case where the sign of the offset distance is changed and the sign of the initial vorticity is kept constant. Therefore, we consider only change in sign of the offset distance and keep the counterclockwise rotation.

The behaviour of the lift coefficients with time for $-1 \geqslant d_{off} \geqslant -4$ is similar to that of the case of $d_{off} = 0$. However, their magnitudes are smaller than that for $d_{off} = 0$ with the same v_{max} and decay exponentially with d_{off} as shown in figure 15. The positive maximum lift coefficient, the negative maximum lift coefficient, and the r.m.s. lift coefficient for $d_{off} \leqslant -1$ are expressed by (20) with $c_1 = 0.942$ and $c_2 = -0.295$, $c_1 = -1.95$ and $c_2 = -0.35$, and $c_1 = 0.74$ and $c_2 = -0.27$, respectively.

The behaviour of the moment coefficients with time for $-1 \geqslant d_{off} \geqslant -4$ is similar to that of the case of $d_{off} = 0$. However, their magnitudes are smaller than that for $d_{off} = 0$ with the same v_{max} and decay with a negative power of $|d_{off}|$ as shown in figure 15. The maximum moment coefficient and the r.m.s. moment coefficient are expressed by (21) with $c_3 = 0.09$ and $m = -1.264$, and $c_3 = 0.0318$ and $m = -1.047$, respectively.

Figure 16(*a*) shows the drag coefficients of the sphere as a function of time for $Re = 100$, $d_{off} = -1$, and $\sigma = 1$. The drag coefficients are obtained with two different maximum fluctuation velocities due to the vortex tube, $v_{max} = 0.1$ and 0.2. The behaviour of the drag coefficients with time is different from that of the case of $d_{off} = 0$. The time-averaged value of the deviation of the drag coefficient from that of the axisymmetric flow past a sphere at each maximum fluctuation velocity is not near zero but is increased linearly in negative value as the maximum fluctuation velocity becomes higher. The minimum drag coefficients occur at about $t = 10$. The minimum drag coefficient and the time-averaged drag coefficient are expressed by (19) with $\beta = -0.78$ and -0.2, respectively.

At about $t = 10$, the centre of the vortex tube is located below the front stagnation point. Thus, the induced velocity due to the vortex tube subtracts its magnitude from the base flow along the stagnation streamline, and so the dynamic pressure ahead of the front stagnation point becomes lower than that of the axisymmetric flow past a sphere. This causes the pressure at the front stagnation point and the shear stresses in the upper and lower left regions to be lower than those of the axisymmetric flow past a sphere. As a consequence, the drag is decreased. From this result, we deduce that if the sphere were free to move rather than fixed, it would experience lower drag than that of a sphere subjected to an axisymmetric flow unless the initial offset distance is large positive. The lower drag will be caused by the upward motion of the sphere owing to the upwash when the vortex tube approaches it, and thus the centre of the vortex tube will be located below the front stagnation point of the sphere. This will cause lower dynamic pressure ahead of the front stagnation point.

Figures 16(*b*)–16(*d*) show the drag coefficients of the sphere as a function of time for $d_{off} = -2$, -3 and -4 with $Re = 100$ and $\sigma = 1$. The minimum drag coefficients occur at about $t = 10$. The minimum drag coefficient $C_{D,min}$ for $d_{off} = -2$ is lower than that

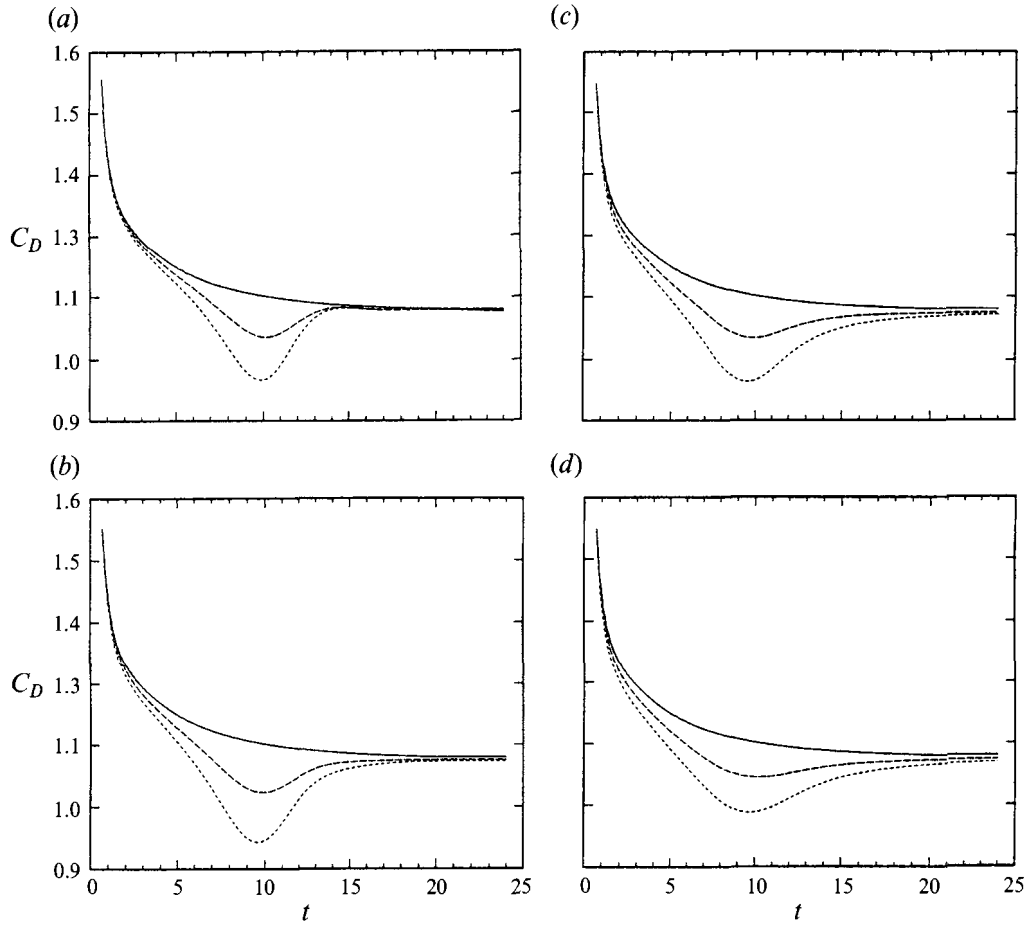

FIGURE 16. Drag coefficients of the sphere as a function of time and v_{max} for (*a*) $d_{off} = -1$, (*b*) -2, (*c*) -3 and (*d*) -4 with $Re = 100$ and $\sigma = 1$. ——, axisymmetric; – – –, $v_{max} = 0.1$; · · · ·, $v_{max} = 0.2$.

for $d_{off} = -1$, because the magnitude of the induced velocity subtracted from the base flow along the stagnation streamline is higher for $d_{off} = -2$ compared to $d_{off} = -1$. The magnitude of $C_{D,min}$ increases as d_{off} decreases below -2. The minimum drag coefficients for $d_{off} = -2$, -3 and -4 are expressed by (19) with $\beta = -0.9$, -0.8 and -0.68, respectively. The time-averaged drag coefficients for $d_{off} = -2$, -3 and -4 are expressed also by (19) with $\beta = -0.28$, -0.3 and -0.29, respectively. We note that the magnitude of the deviation of the drag coefficient from that of the axisymmetric flow decays slowly with d_{off}, in contrast with fast decay of the lift and moment coefficients with d_{off}.

3.4. *Effects of the size of the vortex tube*

We examine the effects of the size of the vortex tube on the flow field by performing computations similar to those in §3.2 for $Re = 100$, $d_{off} = 0$, and five different sizes of the vortex tube, $0.25 \leqslant \sigma \leqslant 4$ in addition to the base case $\sigma = 1$. Each simulation is performed with two different values of $v_{max} = 0.1$ and 0.3.

Table 4 shows the maximum positive lift coefficient, the maximum negative lift coefficient, the r.m.s. lift coefficient, the maximum moment coefficient, and the r.m.s.

v_{max}	$C_{L,max1}$	$C_{L,max2}$	$C_{L,rms}$	$C_{M,max}$	$C_{M,rms}$
			$\sigma = 4$		
0.3	0.337	−0.566	0.307	0.0361	0.0161
0.1	0.113	−0.190	0.102	0.0121	0.00546
			$\sigma = 3$		
0.3	0.338	−0.604	0.299	0.0414	0.0169
0.1	0.114	−0.201	0.0997	0.0139	0.00577
			$\sigma = 2$		
0.3	0.318	−0.611	0.271	0.0455	0.0169
0.1	0.107	−0.203	0.0907	0.0155	0.00593
			$\sigma = 1$		
0.3	0.238	−0.500	0.195	0.0410	0.0138
0.1	0.0810	−0.165	0.0658	0.0145	0.00514
			$\sigma = 0.5$		
0.3	0.147	−0.322	0.119	0.0290	0.00953
0.1	0.0499	−0.106	0.0402	0.0103	0.00355
			$\sigma = 0.25$		
0.3	0.0815	−0.177	0.0660	0.0175	0.00587
0.1	0.0275	−0.0583	0.0221	0.00604	0.00210

TABLE 4. Maximum positive lift coefficient, maximum negative lift coefficient, root mean square of the lift coefficient, maximum moment coefficient, and root mean square of the moment coefficient as a function of v_{max} for six different radii of the vortex tube, $\sigma = 4$, 3, 2, 1, 0.5 and 0.25.

moment coefficient as a function of v_{max} for six different initial radii of the vortex tube, $\sigma = 4$, 3, 2, 1, 0.5 and 0.25. All the coefficients are linearly proportional to v_{max} at each σ. When $\sigma \geqslant 2$, $C_{L,max1}$ and $C_{L,rms}$ become independent of σ, but the magnitudes of $C_{L,max2}$, $C_{M,max}$, and $C_{M,rms}$ for $\sigma = 4$ are smaller than those for $\sigma = 2$ and 3. When σ approaches zero, all the coefficients tend to be proportional to (σv_{max}) which is the circulation of the vortex tube divided by 2π ($\Gamma_v = 2\pi\sigma v_{max}$). For example, $C_{L,rms}$ is expressed by

$$\begin{aligned} C_{L,rms} &= c_1 v_{max} \quad (2 \leqslant \sigma \leqslant 4), \\ &= c_2 v_{max}\sigma^n \quad (0.25 \leqslant \sigma < 2, \quad 0.75 \geqslant n \geqslant 0.5), \end{aligned} \tag{22}$$

where the constant $c_1 = 1$ and $c_2 = 0.65$, and n depends on σ and should approach unity as σ reaches zero. For $C_{L,max1}$, $c_1 = 1.1$ and $c_2 = 0.8$. $C_{L,max2}$, $C_{M,max}$, and $C_{M,rms}$ for $\sigma \leqslant 3$ are also expressed by (22) with $c_1 = -2$ and $c_2 = -1.66$, $c_1 = 0.14$ and $c_2 = 0.14$, and $c_1 = 0.055$ and $c_2 = 0.05$, respectively. The time-averaged value of the deviation of the drag coefficient from that of the axisymmetric flow past a sphere for all values of σ is nearly zero ($O(10^{-4})$).

We note that $C_{L,max2}$, $C_{M,max}$, and $C_{M,rms}$ for $\sigma = 4$ are, respectively, smaller than those for $\sigma = 2$ and 3, and the reason is explained as follows. When the initial size of the vortex core is considerably larger than the sphere size ($\sigma \geqslant 4$), the effect of the shear flow (induced by the passage of the vortex tube) across the sphere diminishes. We explained in §3.2.1 that the magnitude of $C_{L,max2}$ depends on the combined effects of the downwash and the shear flow across the sphere due to the vortex tube. As a result, the magnitude of $C_{L,max2}$ decreases and approaches $C_{L,max1}$ as $\sigma \gg 1$. $C_{M,max}$ and $C_{M,rms}$ also decrease for the same reason. In addition, when the initial size of the vortex core is larger than the sphere size, the effect of the wake behind the sphere on the vortex tube diminishes. As a consequence, the magnitudes of the lift and moment coefficients decay

slowly towards zero after they peak near the time of passage of the vortex tube centre by the plane $z = 1$.

Summarizing the effects of the vortex size, the maximum positive lift coefficient and the r.m.s. lift coefficient depend only on the circulation Γ_v at small values of σ while they depend only on v_{max} (and not σ) at large values of σ. For mid-range values of σ, they depend on both σ and v_{max} (or equivalently both σ and Γ_v).

In §3.3, we investigated the effect of the offset distance on the flow field for $Re = 100$ and $\sigma = 1$. We now examine the effect of initial offset distance of the vortex tube on the lift and moment coefficients of the sphere as a function of the size of the tube at $Re = 100$. The values of $C_{L,max1}$, $C_{L,max2}$, and $C_{L,rms}$ of the sphere for initial offset distance of the vortex tube in the range of $-0.5\sigma^{1/2} \leqslant d_{off} \leqslant \sigma^{1/2}$ are within 5% difference from their values for $d_{off} = 0$. On the other hand, $C_{M,max}$ and $C_{M,rms}$ of the sphere for initial offset distance of the vortex tube in the same range vary by 13% from their values for $d_{off} = 0$.

3.5. *Effects of Reynolds number*

Computations similar to those in §3.2 were performed for four different Reynolds numbers in the range of $20 \leqslant Re \leqslant 80$, $d_{off} = 0$, and $\sigma = 1$ with $v_{max} = 0.2$ in addition to the base case $Re = 100$. We also performed the same calculation with two different values of $v_{max} = 0.1$ and 0.3 and found that $C_{L,max1}$, $C_{L,max2}$, $C_{L,rms}$, $C_{M,max}$, and $C_{M,rms}$ are linearly proportional to v_{max} for each Reynolds number. Figures (17)–(20) show results for $v_{max} = 0.2$.

Figure 17 shows the total maximum positive lift coefficient and the coefficients due to pressure and viscous contributions as a function of Reynolds number for $\sigma = 1$ and $d_{off} = 0$ with $v_{max} = 0.2$. The coefficient due to pressure contribution is a little higher than that due to viscous contribution at Reynolds number 100. Both coefficients due to pressure and viscous contributions increase as the Reynolds number decreases, but the viscous coefficient becomes greater. The total maximum positive lift coefficient increases with a negative power of Reynolds number as Reynolds number decreases, as will be shown in figure 19 on a log–log scale and is expressed by

$$C_{L,max1} = Av_{max} Re^{P}, \tag{23}$$

where the constant $A = 3.5$ and $P = -0.32$.

Figure 18 shows the total maximum negative lift coefficient and the coefficients due to pressure and viscous contributions as a function of Reynolds number for $\sigma = 1$ and $d_{off} = 0$ with $v_{max} = 0.2$. The magnitude of the coefficient due to pressure contribution is 2.38 times higher than that due to viscous contribution at Reynolds number 100. As mentioned in §3.2, the sphere experiences the maximum negative lift coefficient whose magnitude is greater than the maximum positive lift coefficient when the vortex tube passes the sphere, because the vortex tube produces high fluid velocity gradient across the sphere as well as downwash on the sphere. (We note that the shear flow effect induced by the vortex tube would diminish when the size of the vortex tube becomes large.) Thus, the pressure contribution is much higher than the viscous contribution to the total maximum negative lift coefficient. The magnitude of the coefficient due to viscous contributions increases as the Reynolds number decreases, on the other hand, that due to pressure contribution decreases as the Reynolds number decreases. As a consequence, the magnitude of the total maximum negative lift coefficient is not sensitive to the change of the Reynolds number and slowly increases as the Reynolds number decreases.

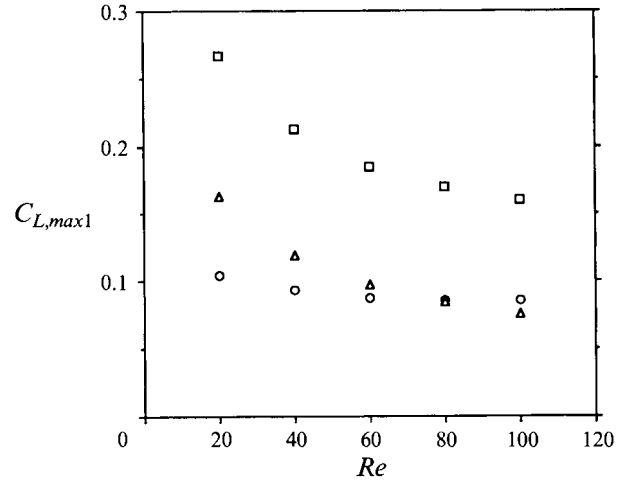

FIGURE 17. Total maximum positive lift coefficient and the coefficients due to pressure and viscous contributions as a function of Reynolds number for $d_{off} = 0$ and $\sigma = 1$ with $v_{max} = 0.2$. □, total; ○, pressure; △, viscous.

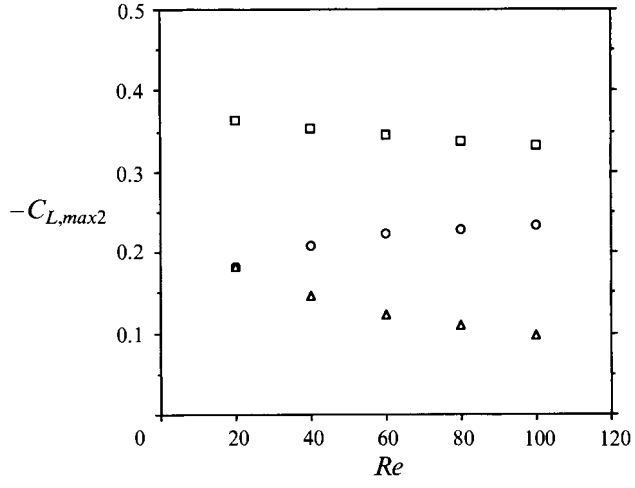

FIGURE 18. Total maximum negative lift coefficient and the coefficients due to pressure and viscous contributions as a function of Reynolds number under the same conditions as figure 17. □, total; ○, pressure; △, viscous.

Figure 19 shows the r.m.s. lift coefficient and also the maximum positive lift coefficient as a function of Reynolds number on a log–log scale for $\sigma = 1$ and $d_{off} = 0$ with $v_{max} = 0.2$. The r.m.s. lift coefficient increases with a negative power of Reynolds number as the Reynolds number decreases and is expressed by (23) with $A = 2.3$ and $P = -0.275$ for $\sigma = 1$. The effect of Reynolds number ($20 \leqslant Re \leqslant 80$) on the lift coefficient was investigated for the vortex size larger than $\sigma = 1$ ($2 \leqslant \sigma \leqslant 4$). The maximum positive lift coefficient and the r.m.s. lift coefficient are linearly proportional only to v_{max} and independent of σ when $\sigma \geqslant 2$ at fixed Reynolds number as in §3.4 for $Re = 100$. The r.m.s. lift coefficient is expressed by (23) with $A = 8.1$ and $P = -0.45$ and written again here for later use.

$$C_{L,rms} = 8.1 v_{max} Re^{-0.45}, \quad 2 \leqslant \sigma \leqslant 4. \tag{24}$$

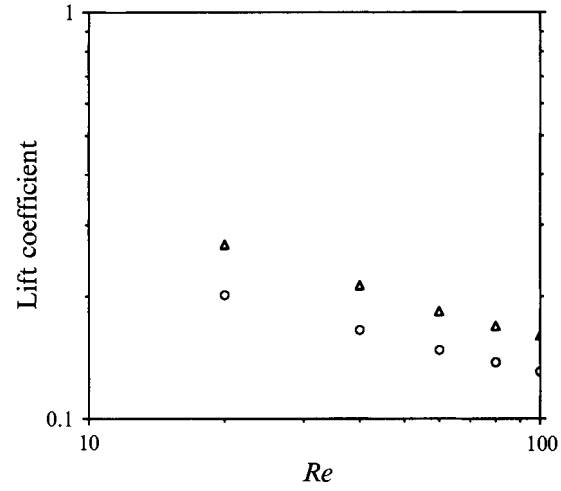

FIGURE 19. Root mean square of the lift coefficient and maximum positive lift coefficient as a function of Reynolds number under the same conditions as figure 17. △, max1; ○, r.m.s.

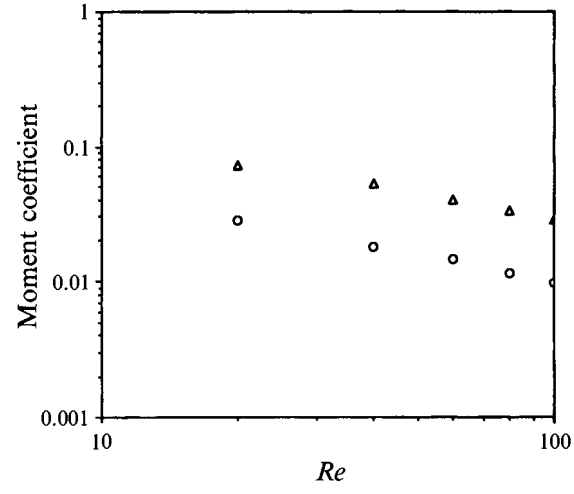

FIGURE 20. Maximum moment coefficient and root mean square of the moment coefficient as a function of Reynolds number under the same conditions as figure 17. △, max; ○, r.m.s.

For the maximum positive lift coefficient, $A = 8.9$ and $P = -0.45$.

Figure 20 shows the maximum moment coefficient and the r.m.s. moment coefficient as a function of Reynolds number for $\sigma = 1$ and $d_{off} = 0$ with $v_{max} = 0.2$. The maximum moment coefficient and the r.m.s. moment coefficient are affected by only the viscous effect and increases with a negative power of Reynolds number as the Reynolds number decreases. $C_{M,max}$ and $C_{M,rms}$ follow the form of (23) with $A = 1.95$ and $P = -0.56$ for the former, and $A = 1.05$ and $P = -0.665$ for the latter for $\sigma = 1$. The effect of Reynolds number ($20 \leqslant Re \leqslant 80$) on the moment coefficient was investigated for $2 \leqslant \sigma \leqslant 4$. The behaviour of the moment coefficient at each Reynolds number is similar to that of the moment coefficient at $Re = 100$ which was explained in §3.4. $C_{M,max}$ and $C_{M,rms}$ follow the form of (23) with $A = 5.5$ and $P = -0.83$ for the former, and $A = 3.1$ and $P = -0.88$ for the latter for $2 \leqslant \sigma \leqslant 3$.

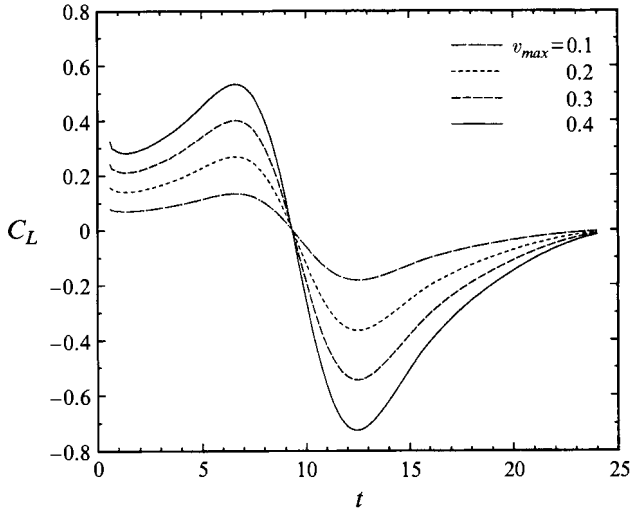

FIGURE 21. Lift coefficients of the sphere as a function of time and v_{max} for $Re = 20$, $d_{off} = 0$ and $\sigma = 1$.

The variation of the lift and moment coefficients for $-0.5\,\sigma^{1/2} \leqslant d_{off} \leqslant \sigma^{1/2}$ from those for $d_{off} = 0$, which is given in §3.4 for $Re = 100$, decreases at fixed σ as the Reynolds number decreases. For example, at $Re = 20$, the difference in the lift coefficient is 4% and that in the moment coefficient is 10%.

We investigate the lift, moment and drag coefficients at Reynolds number 20 in order to find out about the Reynolds number effect in more detail. Figure 21 slows the lift coefficients of the sphere as a function of time for $Re = 20$, $d_{off} = 0$, and $\sigma = 1$. The lift coefficients are obtained with four different maximum fluctuation velocities due to the vortex tube, $v_{max} = 0.1, 0.2, 0.3$ and 0.4. The maximum positive lift coefficient $C_{L,max1}$ occurs at $t = 6.6$, and the maximum negative lift coefficient $C_{L,max2}$ occurs at $t = 12.5$. The lift coefficient is linearly proportional to the maximum fluctuation velocity (or the circulation of the vortex tube) at each time over the whole time computed ($0 \leqslant t \leqslant 24$). This shows that the nonlinear effect at $Re = 20$ is much less than that at $Re = 100$. In contrast to figure 13 which shows the lift coefficient for $Re = 100$, figure 21 shows that the lift coefficient decays slowly to zero after it attains the maximum negative value. This indicates that for $Re = 100$ viscous diffusion in the wake is much stronger than that in the upstream; on the other hand, viscous diffusion is uniformly important all around the sphere at $Re = 20$ compared to $Re = 100$. The behaviour of the moment and drag coefficients with time is similar to that of the case of $Re = 100$. The time-averaged lift and moment coefficients are nearly zero ($O(10^{-2})$ and $O(10^{-3})$, respectively), and the time-averaged drag coefficient is close to that of the axisymmetric flow without the vortex tube (the difference between them is $O(10^{-2})$).

One of the reviewers noted that some of our results can be explained using dimensional analysis as follows. The lift force on the sphere can be expressed in a functional form as

$$F'_L(t') = f(U'_\infty, \rho', \mu', a'_0, \Gamma', \sigma', d'_{off}; t').$$

From dimensional analysis, it follows that

$$C_L(t) = \frac{F'_L}{\frac{1}{2}\rho' U'^2_\infty \pi a'^2_0} = f\left(\frac{\sigma'}{a'_0}, \frac{U'_\infty \sigma'}{\Gamma'}, \frac{\mu'}{\rho' U'_\infty a'_0}, \frac{d'_{off}}{a'_0}; \frac{t' U'_\infty}{a'_0}\right) = f(\phi_1, \phi_2, \phi_3, \phi_4; t),$$

where ϕ_i are the four parameters appearing on the left-hand side of the last equal sign. If Reynolds number and the dimensionless offset distance are fixed, $C_L(t)$ will be a function of ϕ_1, ϕ_2, and t. Furthermore, when σ'/a_0' is small, we expect that a_0' is more important than σ'. Then C_L should be a function only of ϕ_1/ϕ_2 and t yielding:

$$C_L(t) = f\left(\frac{\Gamma'}{U_\infty' a_0'}; t\right) = f(\Gamma; t). \tag{25}$$

In the opposite limit, a_0' should be unimportant and

$$C_L(t) = f\left(\frac{\Gamma'}{U_\infty' \sigma'}; t\right) = f(v_{max}; t). \tag{26}$$

Equations (25) and (26) are consistent with our results in §3.4.

Finally, we discuss the effect of the initial location of the vortex tube upstream from the centre of the sphere. We have shown earlier that the maximum positive lift coefficient is expressed at given σ and Re as $C_{L,max1} = cv_{max}$ when the initial location of the vortex, l, is 10 radii. From a different initial location, say l^*, the equation for the maximum positive lift coefficient should be modified as follows.

$$\begin{aligned} C_{L,max1} &= cv_{max} \\ &= c\frac{\sigma^*}{\sigma} v^*_{max} \\ &= c\left(1 - \frac{10.04(l^* - l)}{Re\,\sigma^2}\right)^{1/2} v^*_{max} \\ &= c^* v^*_{max}, \end{aligned} \tag{27}$$

where we used $v_{max}/v^*_{max} = \sigma^*/\sigma$ and $\sigma^{*2} - \sigma^2 = 10.04\,(l^* - l)/Re$, which are obtained from the evolution of a point vortex in a viscous fluid (Batchelor 1967). v^*_{max} denotes the maximum fluctuation velocity due to the vortex tube whose initial location is l^* radii upstream from the centre of the sphere. Note that the proportionality constant c is now modified as c^* for the new initial location of the vortex l^*

We examined the accuracy of (27) by performing computations for $l^* = 8$ and 12 with the same parameters as used in §3.2.1 except the initial location of the vortex tube. The magnitude of $C_{L,max1}$ obtained from (27) differs by 0.2% from that of the full computations. The equation of the r.m.s. lift coefficient should also be modified as (27) for the new initial location of the vortex tube. In addition, the time span, t_{ave}, over which averaging the lift coefficient is performed should be modified according to $t^*_{ave} = t_{ave} + (l^* - l)$.

4. Conclusions

As a first step towards better understanding the physics of interaction between a particle and the turbulent carrier flow, we have investigated numerically the unsteady, three-dimensional, incompressible, viscous flow interactions between a vortical (initially cylindrical) structure advected by a uniform free stream and a spherical particle suddenly placed and held fixed in space for a range of particle Reynolds numbers $20 \leqslant Re \leqslant 100$. The counterclockwise rotating cylindrical vortex tube is initially located ten sphere-radii upstream from the centre of the sphere.

A summary of our findings and their applications is provided as follows.

(i) One significant finding in our study is that the r.m.s. lift coefficient for a particle is linearly proportional to the upwash (or downwash) induced by the vortex tube motion on the particle normal to the direction of the free stream in our case (or the direction of the particle motion in the case of a free particle) and is independent of the size of the vortex tube when the size of the vortex is greater than that of the particle, $2 \leqslant \sigma \leqslant 4$. This result can be applied to turbulent flows containing small concentration of particles in order to obtain the r.m.s. lift force on a particle. A turbulent flow possesses a wide spectrum of eddy sizes. The large eddies contain most of the turbulent kinetic energy and produce high-velocity fluctuations, and so they are responsible for the dispersion of particles. The particle size, at the extremes, may be comparable to either the integral lengthscale or to the Kolmogorov lengthscale. When the size of particle is comparable to the integral lengthscale, the r.m.s. lift coefficient of the particle is obtained by (24). Furthermore, our results tend to support the idea that (24) would be applicable to the case of an eddy much larger than the particle. Thus, when the size of particle is comparable to the Kolmogorov lengthscale, the r.m.s. lift coefficient of the particle can be calculated approximately by (24), where v_{max} is the maximum velocity fluctuation due to an eddy of size comparable to the integral lengthscale. The time during which the particle is influenced by the eddy is of the order of the eddy life time.

The deflection of the particle path will depend on the magnitude of the r.m.s. lift coefficient and the ratio, ρ_r, of the particle density to that of the carrier fluid ($C_L = \frac{8}{3}\rho_r A$, where A is the dimensionless acceleration of the particle due to the lift force). This result provides a simple method to estimate the deflection of particle trajectory in the dilute particle-laden turbulent flow. Equation (24) and the non-dimensionalized Newton's second law show that the deflection increases slowly as the Reynolds number of the particle decreases.

(ii) The magnitude of the r.m.s. moment coefficient of the particle is one order of magnitude less than that of the r.m.s. lift coefficient when $Re \geqslant 20$. Furthermore, when the initial size of the vortex core is considerably larger than the sphere size ($\sigma \geqslant 4$), the effect of the shear flow (induced by the passage of the vortex tube) across the sphere diminishes and the torque on the particle decreases. Thus, the torque on the particle might be negligible in many applications.

(iii) When a vortex tube advected by a uniform free stream approaches a sphere, the sphere experiences lower drag than that of a sphere subjected to an axisymmetric flow if the sphere were free to move rather than fixed, unless the initial offset distance of the vortex tube is large positive, as explained in §3.3.2. The lower drag is caused by the upward motion of the sphere due to the upwash of the approaching vortex tube, and thus the centre of the vortex tube would be located below the front stagnation point of the sphere. This causes lower dynamic pressure ahead of the front stagnation point.

(iv) Some interesting unsteady phenomena in the near wake have been discovered. The shape of the near wake behind the spherical particle is controlled by the pressure difference between the top and bottom of the near wake as was indicated by Kim *et al.* (1993). The instantaneous flow patterns around a spherical particle in a turbulent flow would include some of those described in this paper. For example, our recent results (to be published), from a study of the interactions between a vortex pair advected by a uniform free stream and a sphere, show that the streamlines are similar to those described in the present paper.

We are also studying the heat and mass transfer for a droplet interacting with an array of vortices in high-temperature and high-pressure environments such as that in a gas turbine combustor.

This work has been supported by the Air Force Office of Scientific Research under grant no. F49620-93-1-0028 with Dr Julian Tishkoff acting as the technical monitor. We would like to thank Mr Lyle Wiedeman for his assistance in using a three-dimensional graphic package Application Visualization System (AVS). The support of the San Diego Supercomputer Center and the San Diego supercomputer Centre under a block grant of the Office of Academic Computing of UCI is appreciated.

REFERENCES

ANDERSON, D. A., TANNEHILL, J. C. & PLETCHER, R. H. 1984 *Computational Fluid Mechanics and Heat Transfer*. Hemisphere.

BASSET, A. B. 1988 *A Treatise on Hydrodynamics*, vol. 2, p. 285. Dover.

BATCHELOR, G. K. 1967 *An Introduction to Fluid Dynamics*, p. 201. Cambridge University Press.

CLIFT, R., GRACE, J. R. & WEBER, M. E. 1978 *Bubbles, Drops, and Particles*. Academic.

HOUGHTON, G. 1963 The behaviour of particles in a sinusoidal velocity field accelerating in a viscous fluid. *Proc. R. Soc. Lond.* **272**, 33–43.

INGEBO, R. D. 1956 Drag coefficient and relative velocity in bubbly, droplet, or particulate flows. *NASA TN* 3762.

KIM, I., ELGHOBASHI, S. & SIRIGNANO, W. A. 1993 Three-dimensional flow over two spheres placed side by side. *J. Fluid Mech.* **246**, 465–488.

MCLAUGHLIN, J. B. 1991 Inertial migration of a small sphere in linear shear flow. *J. Fluid Mech.* **224**, 261–274.

MAXEY, M. R. & RILEY, J. J. 1983 Equation of motion for a small rigid sphere in a nonuniform flow. *Phys. Fluids* **26**, 883–889.

ODAR, F. 1966 Verification of the proposed equation for calculation of the forces on a sphere accelerating in a viscous fluid. *J. Fluid Mech.* **25**, 591–592.

PATNAIK, G. 1986 A numerical solution of droplet vaporization with convection. PhD dissertation, Carnegie-Mellon University.

PATNAIK, G., SIRIGNANO, W. A., DWYER, H. A. & SANDERS, B. R. 1986 A numerical technique for the solution of a vaporizing fuel droplet. *Prog. Astro. Aero.* **105**, 253–266.

RUBINOW, S. I. & KELLER, J. B. 1961 The transverse force on a spinning sphere moving in a viscous fluid. *J. Fluid Mech.* **12**, 447–459.

SAFFMAN, P. G. 1965 The lift on a small sphere in a slow shear flow. *J. Fluid Mech.* **22**, 385–400.

SAFFMAN, P. G. 1968 The lift on a small sphere in a slow shear flow – Corrigendum. *J. Fluid Mech.* **31**, 624.

SCHÖNEBORN, P. R. 1975 The interaction between a single particle and an oscillating fluid. *Int. J. Multiphase Flow* **2**, 307–317.

SPALART, P. R. 1982 Numerical simulation of separated flows. PhD thesis, Stanford University.

TANEDA, S. 1956 Experimental investigation of the wake behind a sphere at low Reynolds number. *J. Phys. Soc. Japan* **11**, 1104–1108.

VINOKUR, M. 1983 On one-dimensional stretching functions for finite-difference calculations. *J. Comput. Phys.* **50**, 215–234.